Chemical Science

ROYAL SOCIETY OF CHEMISTRY

REVIEW

View Article Online
View Journal | View Issue

Cite this: *Chem. Sci.*, 2025, **16**, 17568

Single-atom catalysts meet electrospinning: a blissful marriage for energy catalysis

Bingyan Shi and Xiaofeng Lu *

Received 5th May 2025
Accepted 1st September 2025

DOI: 10.1039/d5sc03248b

rsc.li/chemical-science

Since the introduction of the concept of single-atom (SA) catalysis, numerous SA catalysts (SACs) with exceptional catalytic performance have been developed. Electrospinning represents a powerful technique for fabricating nanofibrous materials, characterized by high porosity, distinct electron/mass transfer properties, self-supporting capability, and low density. Consequently, integrating SACs with electrospun nanofibers (ENFs) harnesses their structural advantages, thereby augmenting catalytic efficacy. This review examines the concept of SA-ENFs, underscoring the synergy between the nanosized support architecture and atomic-level catalysts, which collectively offer abundant catalytically active sites. Furthermore, the well-defined spatial arrangement of nanofibers combined with highly efficient SAs imparts unique electron transfer and electrolyte transport capabilities, thereby promoting the catalytic performance. Herein, a detailed understanding of the influence of the coordination environment and the interactions between multiple active sites within ENFs on the electrocatalytic performance is highlighted. This review also identifies potential challenges facing this novel class of SA-ENFs in electrocatalytic applications.

1. Introduction

Single-atom catalysts (SACs) harness individual atoms as the active centers in catalytic reactions, markedly reducing the activation energy barrier. To ensure structural stability, SACs are typically anchored onto robust carriers that enable strong interactions, such as metals, metal oxides, carbon-based materials, and molecular sieves. The concept of isolated atoms with titanium (Ti) sites was initially spotlighted in 1995 through the binding of metallocene complexes to mesoporous silica, which was employed for the epoxidation of cycloolefin.[1] In 1999, atomically dispersed platinum (Pt) supported on MgO, derived from the pyrolysis of $Pt(acac)_2$ under an O_2/helium (He) atmosphere, was shown to catalyze the combustion of acetone with efficacy comparable to that of metallic Pt particles.[2] In 2011, Zhang *et al.* successfully demonstrated the fabrication of a SAC consisting of atomically dispersed Pt on FeO_x nanocrystals for the CO oxidation reaction, realizing a remarkable atom efficiency, exceptional robustness, and superior catalytic activity.[3] Theoretical findings indicate that this enhanced catalytic performance stems from the highly active, high-valent Pt atoms, which weaken the CO adsorption and facilitate the activation process, significantly advancing the mechanism understanding of SACs. SACs showcase atomic-level catalytic activity, distinguishing them from traditional nanocatalysts through unique surface reactivity and size-dependent effects.

SACs hold significant promise in bridging the gap between homogeneous and heterogeneous catalysis, achieving an ultra-high atomic utilization efficiency coupled with robust environmental stability and unparalleled catalytic performance. Within SACs, the metal sites are typically coordinated by specific nonmetal atoms such as nitrogen (N), carbon (C), sulfur (S), phosphorus (P), *etc.* in the support matrix, exhibiting a partially positive charge. This distinct electronic structure fosters a synergistic interaction between the single atom (SA) and the support that influences the binding of reactants, intermediates and products, enhancing both catalytic activity and selectivity.[4] Consequently, the size of the support plays a pivotal role in the catalytic properties of SACs. For instance, optimized CeO_2 carrier size modulates the interface between metal atoms and CeO_2, significantly boosting CO oxidation catalytic activity.[5] Recent years have witnessed rapid development in constructing diverse SACs for pivotal catalytic reactions, spanning chemical catalysis, environmental catalysis, enzyme catalysis, photocatalysis and electrocatalysis.[6–8] For example, atomically dispersed palladium (Pd) on a TiO_2 catalyst with 1.5% Pd loading has been prepared *via* a photochemical strategy, showing 9- and 55-fold enhanced catalytic hydrogenation activity for alkenes and aldehydes, respectively.[9] Iron (Fe) single-atom (SA)/g-C_3N_4 nanotubes have been demonstrated to be an efficient Fenton-like catalyst, exhibiting an ultrahigh catalytic efficiency that is 75 times superior to that of pristine g-C_3N_4.[10] In the realm of formate oxidase (FOD) catalysis, Pd SA assembly presents a markedly better FOD-like performance, with a hydrogen peroxide (H_2O_2) production rate of 22.86 mol g_{Pd}^{-1} h^{-1} and superior selectivity,

Alan G. MacDiarmid Institute, College of Chemistry, Jilin University, Changchun, 130012, P.R. China. E-mail: xflu@jlu.edu.cn

greater surpassing Pd nanoparticles (NPs).[11] Interestingly, a Pt SA/C_3N_4 catalyst has also been demonstrated to possess exceptional photocatalytic properties for water splitting with a notable H_2 production rate of 1.66 mmol h^{-1} mg^{-1} Pt, which is 5.9-fold higher than that of Pt NPs/C_3N_4.[12] In a representative electrocatalytic application, Bi SAs anchored on porous Bi_2O_{3-x} nanosheets have been explored to display exceptional electrocatalytic performance towards CO_2 reduction, delivering a significant faradaic efficiency (FE) of 96.48% in alkaline electrolyte and 92.26% under neutral conditions for formate, while maintaining exceptional durability.[13]

Electrospinning stands out as a distinctive fiber manufacturing technology that harnesses high voltage electricity to create fibers through the exciting electrostatic atomization of polymer fluids.[14] The typical electrospinning apparatus comprises three essential components: a high-voltage power supply, a spinneret and a collector.[15] During the electrospinning process, a droplet formed at the spinneret tip undergoes a sharp transformation from spherical to conical shape under a potent electrical field, forming what is commonly referred to as Taylor cones.[16] Subsequently, the polymer solution is stretched into fine jets from the Taylor cones, which solidify into fibers through solvent evaporation or cooling to a proper temperature as they travel toward the collector. The electrospinning technique has evolved over nearly a century since its initial proposal in 1932. To date, a diverse array of polymers, metals, ceramics, carbons, and composites have been successfully electrospun to yield their respective nanofibrous architectures.[17–20] Intriguingly, beyond conventional solid nanofibers, the refined electrospinning technique, either with or without post-treatment assistance, also enables the fabrication of hollow nanotubes, core–shell nanostructures, hierarchical architectures, and even Janus nanostructures.[19,20] These nanomaterials exhibit precisely controllable architectures and compositions, conferring distinct advantages including high specific surface area, tunable surface physicochemical properties, and superior electron/mass transfer capabilities.[21] Consequently, they demonstrate promising utility across diverse applications such as selective separation and filtration, electromagnetic shielding, thermal insulation, electrocatalysis, adsorption, and antibacterial systems.[22]

In particular, electrospun nanofibers (ENFs) demonstrate extensive utility in energy catalysis.[23–26] Representative examples include manganese (Mn)-doped RuO_2 nanofibers, which leverage distinct nanofibrous morphology and doping effects to optimize the electronic structure.[27] The catalyst exhibits exceptional bifunctional performance for both hydrogen and oxygen evolution reactions (HER/OER) in alkaline electrolyte at industrial-level current densities. When configured as an integrated water splitting electrolyzer, a remarkably low cell voltage of only 1.44 V is achieved to drive a current density of 10 mA cm^{-2}, with operational stability exceeding 55 hours. Furthermore, substituting the OER with alternative nucleophile oxidation pathways substantially enhances HER-driven H_2 production efficiency in an electrocatalyst comprising NiS-coated Ni-carbon nanofibers (CNFs) with low-content Pt species.[28] ENFs further function as electrochemical electrodes in battery systems, enabling cost-effective renewable energy deployment. In particular, their three-dimensional (3D) electrodes with tailored compositions simultaneously establish rapid mass-transfer pathways and enrich reaction sites, enhancing electrochemical performance.[29]

Building upon these foundations, integrating SAs with ENFs represents a promising paradigm for advanced energy catalysis. Significant research efforts have already been directed toward this synergistic approach. In this review, we have presented the latest advancement in the fabrication of SA-ENFs and their potential in energy-related catalytic applications. These engineered materials offer distinct advantages, including maximized atom utilization efficiency, abundant accessible active sites, interfacial electric field gradient modulation for activity control, and enhanced electron and mass transfer properties. Herein, we systematically delineate the prevalent synthesis methodologies for SA-ENFs and evaluate their performance across critical energy catalytic domains, including the HER, OER, oxygen reduction reaction (ORR), hydrogen oxidation reaction (HOR), CO_2RR, nitrate reduction reaction (NO_3RR), and battery/electrolysis technologies such as zinc (Zn)–air batteries, fuel cells, overall water splitting, and Li batteries (Fig. 1). Special emphasis is placed on elucidating structure–activity relationships between the atomic coordination environment, multi-site interactions within ENF matrices, and the resultant electrocatalytic performance. This integrated SA-ENF design framework provides fundamental insights for developing next-generation high-performance electrocatalysts.

2. Scientific significances of SA-ENFs

ENFs possess intricate spatial structures, which are particularly beneficial for the selective encapsulation of individual atoms.

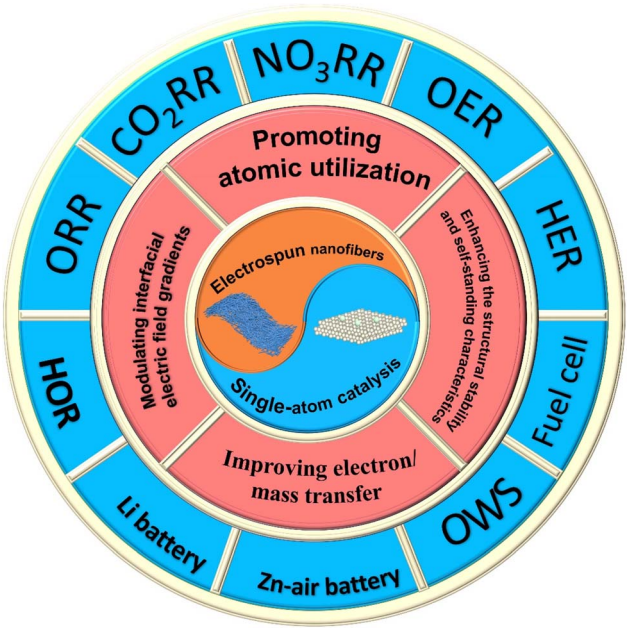

Fig. 1 A scheme of the synergistic SACs/ENF integration strategy with significant advantages for energy catalysis.

Upon incorporation, SAs become stabilized within the fiber matrix through metal-nonmetal bonding, effectively modulating surface chemistry and enhancing atomic-level catalytic efficacy. This interaction between SAs and ENFs leverages distinctive spatial configurations and electronic interactions to deliver near-theoretical atomic utilization efficiency, uniform spatial distribution of active sites, and promoted electron and mass transfer kinetics. Collectively, these attributes significantly elevate electrocatalytic performance beyond conventional catalyst design.

2.1 Promoting atomic utilization through the nanofiber-confinement effect

SA stabilization typically requires atomic dispersion within support matrices, where the coordination environment critically determines electrocatalytic efficiency. ENFs, characterized by their distinctive spatial structure and sub-micron diameters, are adept at confining active components to achieve maximal atomic exposure and near-unity atomic utilization. To augment surface area and uncover additional active sites, constructing porous nanofibers represents a strategic approach. For example, N-doped porous CNFs (NPCNFs) have been synthesized through the carbonization of polyacrylonitrile (PAN) nanofibers containing zeolite imidazole framework (ZIF-8) NPs.[30] During pyrolysis, ZIF-8 decomposition simultaneously generates microporosity in CNFs and enables N-doping. This dual functionality efficiently traps the Pt precursor to form Pt SAs through anchoring with N and C atoms during the subsequent thermal treatment. The resulting porous nanofibrous structure boasts a high Pt-loading (2.33 wt%) while providing abundant Pt–N_2C_2 active sites for the HER, ultimately delivering a superior electrocatalytic performance compared to commercial Pt/C benchmarks.

2.2 Improving electron/mass transfer properties

The unique coordination environment of SACs enables precise electronic structure modulation and facilitates efficient electron transfer during electrocatalytic processes, and then SA-ENFs themselves form a continuous electronic highway network throughout the entire electrode.[31,32] This provides the nanofibrous system with a parallel and non-interfering electron transport pathway. Particularly in multi-component catalytic reactions, synergistic effects often involve electron transfer between distinct sites. The highly efficient axial electron conduction along the nanofibers rapidly balances the charge states between different sites, facilitating the interfacial charge transfer process and enabling multi-component synergistic catalysis.[33] In contrast, the inter-fiber gaps and the pores/channels within the porous fibers constitute continuous ion transport pathways.[34] In particular, open-ended N-doped multichannel CNFs (NMCNFs) have been used to immobilize molybdenum (Mo) SAs, which shorten the mass-transfer pathways and allows for a rapid access to the reactive sites.[35] The multichannel configuration further promotes H_2 desorption, thereby accelerating the electrocatalytic reaction kinetics. Beyond porous architectures, aligned nanofibers exhibit directional order that markedly enhances mass transfer. In a flow cell configuration, aligned CNFs greatly outperform randomly oriented counterparts by facilitating superior reactant/product diffusion, thereby boosting H_2O_2 electrosynthesis performance.[36] Collectively, the efficient axial electron/ion transport allows reactant molecules to be captured at adsorption centers and also rapidly transferred to catalytic sites, greatly accelerating the electrocatalytic conversion process.

2.3 Enhancing structural stability and self-standing characteristic

SACs offer the distinct advantages of maximum atomic utilization and high intrinsic reactivity. However, the considerably increased surface free energy often compromises structural stability, posing a major challenge for practical electrocatalytic applications. To enhance the structural stability of SACs, several efficacious routes have been developed, including reducing the mobility of SAs on the carrier through the steric hindrance, manipulating coordination environments, and strengthening metal site–support interactions. Confinement within ENFs further improves the structural stability of SACs through the regulation of the chemical bonding. Studies demonstrate that Fe SAs immobilized within NCNFs with a four N atom coordination configuration yield superior structural integrity compared to samples with fewer coordination numbers of N.[37]

Furthermore, the self-standing nature of ENFs offers additional structural stability benefits, enabling their direct deployment as binder-free electrodes for electrocatalytic applications.[38] Notably, the inherent flexibility of the ENF membranes enables them to retain cooperative active-site behavior even under mechanical deformation. Typically, an Fe SA electrocatalyst featuring Fe–N_5 moieties immobilized on NMCNFs demonstrates exceptional ORR properties due to the presence of an axial N ligand for modulating the electronic structure of the Fe site to optimize intermediate adsorption.[39] Crucially, the mechanical flexibility of the catalyst enables the assembled Zn–air battery to maintain exceptional structural integrity and electrochemical performance under bending conditions even at 90° angle. Moreover, this flexible characteristic of the ENF membranes allows for the direct fabrication of fiber-shaped batteries capable of powering wearable electronics, demonstrating substantial potential for practical applications.[40]

2.4 Modulating interfacial electric field gradients

In heterostructures, polarization effect and interfacial electron transfer between dissimilar components generate a built-in electric field. This field gradient modulates catalytic intermediate adsorption, facilitating electrocatalytic reactions by reducing energy barriers. Notably, atomically asymmetric local electric field gradients can be engineered in the dizygotic SAC system, reaching an intensity of 4.0×10^{10} N/C.[41] This configuration shortens the active site–H bond lengths and optimizes water orientation, significantly enhancing the alkaline HER performance. In a typical Fe SA-ENF system, the asymmetric N/P coordinated Fe sites (Fe–N_3P_1) exhibit higher charge density

than symmetric N_4-coordinated Fe sites.[42] This charge asymmetry generates interfacial electric field gradients that weaken *O and *OH adsorption while stabilizing *OOH adsorption, thereby improving both ORR and OER efficiencies. Collectively, these findings demonstrate how strategically engineered local electric field gradients optimize reaction pathways, which is a design principle extendable to diverse electrocatalytic processes.

3. Fabrication strategies of SA-ENFs

3.1 Functional material- and small molecule-assisted approach

3.1.1 MOF-assisted pyrolysis. High-temperature pyrolysis represents a highly efficient way to construct SAs within carbon barriers. During thermal treatment, nonmetal atoms coordinate with the metal atoms, leveraging their lone pair electrons. Metal organic frameworks (MOFs) typically feature a wealth of organic ligands rich in nitrogen and carbon, which serve to coordinate metal ions. When incorporated into polymeric ENFs, this configuration enables dual confinement of single metal atoms by both MOF ligands and the polymer matrix during pyrolysis, ensuring uniform SA distribution within CNFs.[30,43–45] Concurrently, the templating effect of MOFs endows the SAs/CNFs with hierarchical porosity and high specific surface area, which are critically advantageous for the electrocatalytic reactions. For example, Ni SAs immobilized within porous CNFs have been developed by incorporating Ni-ZIF8 into electrospun PAN/poly(methylmethacrylate) (PMMA) nanofibers, followed by high-temperature pyrolysis under an inert atmosphere.[44] This process simultaneously generates catalytically active Ni–N_4 moieties while volatilizing low-melting-point PMMA to create abundant mesopores. The resulting Ni SA/CNFs present a substantial specific surface area of 688.3 $m^2\ g^{-1}$, predominantly featuring mesopores ranging from 2 to 50 nm. This well-engineered porous architecture facilitates gas mass transport while maximizing exposure of Ni–N_4 active sites, collectively enabling highly active and selective electrocatalytic CO_2 reduction to CO.

3.1.2 Functional compound- and polymer-assisted treatment. Functional compounds and polymers enriched with N, P and S functionalities readily coordinate with metal centers to form SACs. Dicyandiamide (DCDA), a prominent N-rich compound, serves as an effective precursor for establishing metal–N bonds during pyrolysis. Electrospinning a polymeric solution containing PAN, DCDA and Ni salt yields uniform nanofibers, with subsequent carbonization generating Ni SAs immobilized within NCNFs.[46] The synergistic combination of PAN and DCDA offers a high-concentration N source that facilitates Ni coordination to form Ni SACs. Fourier transformation (FT)-extended X-ray absorption fine structure (EXAFS) spectroscopy confirms the formation of Ni–N_3 moieties, enhancing the electrocatalytic CO_2RR. Beyond small-molecule precursors, N/S/P-containing polymers such as polyaniline, polypyrrole, polythiophene and polydopamine are also viable candidates for stabilizing SAs during thermal/reductive treatment,[47,48] establishing polymer-assisted pyrolysis as a viable route for synthesizing SACs within ENFs. Notably, recent studies demonstrate that polyaniline can directly stabilize Pt SAs without requiring pyrolysis, enabling facile construction of SAs within the polymer matrix.[49]

3.1.3 SiO_2-assisted pyrolysis. SiO_2 enables spatial isolation to engineer the coordination of metal atoms with N/P/S groups for SAC synthesis. Acting as dual-function templates, SiO_2 NPs simultaneously isolate metal species and generate porous architectures upon etching.[34,50] Illustratively, Mo SAs have been successfully anchored within NMCNFs as an efficient HER electrocatalyst (Fig. 2a).[35] During the electrospinning process, tetraethyl orthosilicate (TEOS) is introduced into the precursor solution containing PAN and Mo salt. Following pyrolysis, TEOS decomposes into SiO_2 NPs, leading to the formation of atomic-level Mo sites on NMCNFs. Subsequent alkaline etching removes the SiO_2 NPs to yield open-ended multichannel nanofibers (Fig. 2b–d). Aberration-corrected high-angle annular dark-field scanning transmission electron microscopy (AC HAADF-STEM) and elemental mapping confirm the uniform distribution of Mo SAs within NMCNFs (Fig. 2e and f). The N_2 adsorption–desorption isotherms reveal a porous structure with a Brunauer–Emmett–Teller (BET) surface area of 274.4 $m^2\ g^{-1}$ (Fig. 2*g*). This configuration enhances active site accessibility and charge transfer efficiency, reducing activation energy barriers and accelerating electrocatalytic kinetics. FT-EXAFS and Mo K-edge EXAFS fitting analyses identify the establishment of Mo–$O_1N_1C_2$ coordination as the active sites responsible for the exceptional HER properties (Fig. 2h–j).

3.1.4 Zn source-assisted pyrolysis. The low boiling point of zinc (Zn) facilitates evaporation during high-temperature pyrolysis, enabling ZnO-assisted synthesis of SACs.[51] During a high-temperature treatment of Fe-doped ZnO and Ni-doped ZnO on a ZIF-8 material, ZnO is reduced to metallic Zn, which then evaporates, allowing for the formation of Fe/Ni SA pairs immobilized within N-doped carbon derived from ZIF-8. Similarly, ZnS serves as an alternative Zn source for aiding the formation of SACs. During the electrospinning process, ZnS nanospheres are dispersed in electrospun PAN/$Fe(NO_3)_3$ nanofibers. Following a pyrolysis treatment, ZnS nanospheres decompose at a high temperature to produce hierarchical pores while introducing S dopants within the PAN-derived CNFs and immobilizing Fe SAs. FT-EXAFS analysis confirms exclusive Fe–N/O bonding (absent Fe–Fe/Fe–S bonds) in the resulting product. The synergistic S doping enhances electron/mass transfer kinetics, significantly boosting electrocatalytic performance in both the ORR and OER.[52] Recently, zinc acetate has been directly used to construct edge-located Fe SACs *via* a thermal etching approach, which simultaneously produces mesopores and micropores, benefitting from active sites exposure and rapid mass transfer.[53]

3.1.5 NH_3-assisted graphitization process. The NH_3-assisted synthesis approach is widely employed for preparing SACs, particularly supported SACs. This strategy typically involves combining a metal precursor (*e.g.*, metal salts) with a support material (*e.g.*, carbon-based materials or oxides). NH_3 fulfills two pivotal roles in this synthetic process. Initially, it functions as a reducing agent that decomposes at elevated temperatures to yield H_2, which in turn reduces metal ions to their metallic

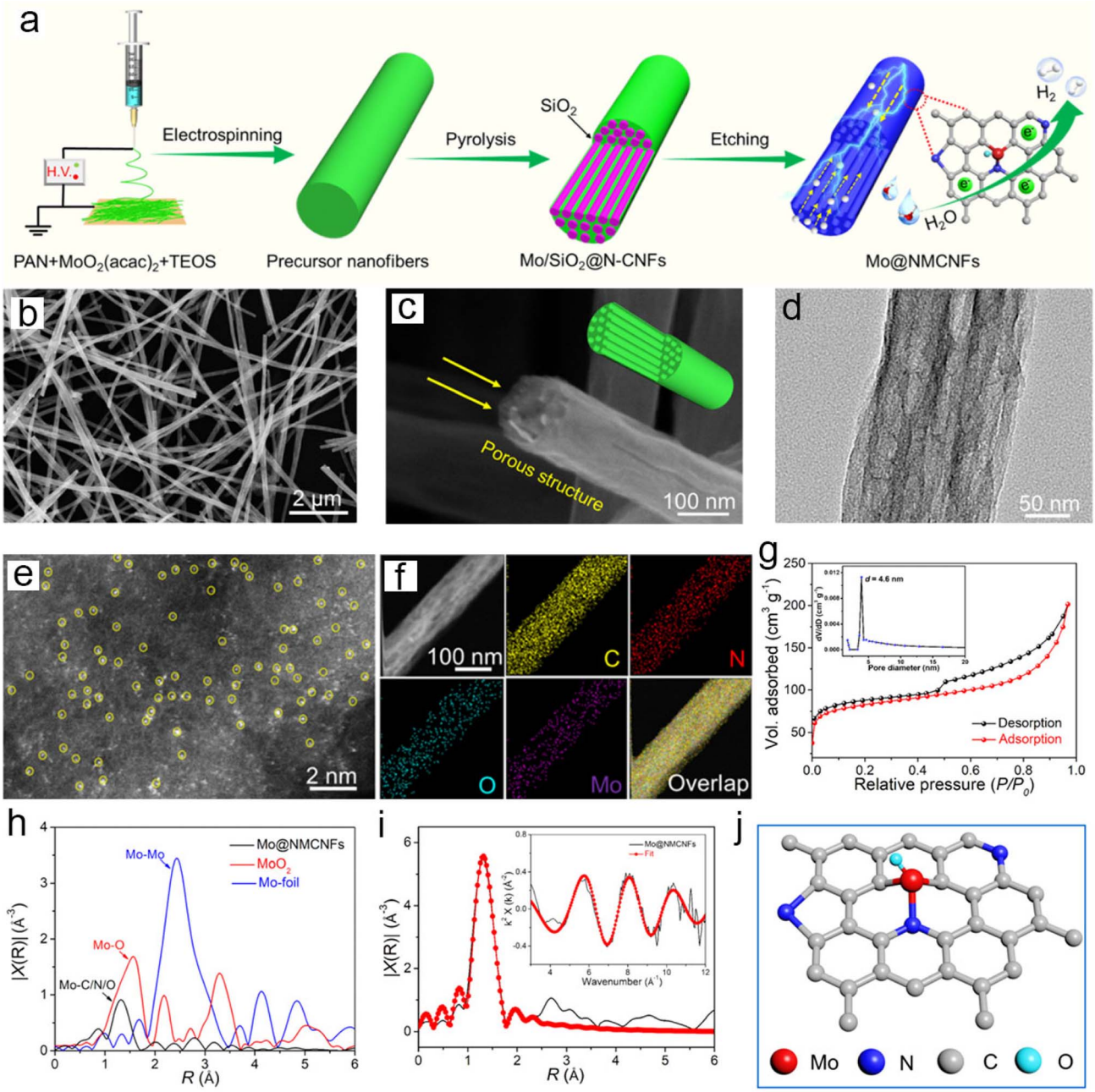

Fig. 2 (a) A scheme for constructing Mo SAs anchored on NCNFs. (b) and (c) SEM images, (d) TEM image, (e) AC HAADF-STEM image, (f) HAADF-STEM image and elemental mapping of Mo SAs loaded on NCNFs. (g) N_2 adsorption–desorption isotherms and pore size distribution of the catalyst. (h) FT-EXAFS curves of varied samples. (i) Mo K-edge EXAFS and the *k*-space fitting curves for the catalyst. (j) Assessment of the Mo–$O_1N_1C_2$ coordination environment. Reproduced with permission.[35] Copyright 2021, American Chemical Society.

SAs. Subsequently, it serves as a coordination agent, which complexes with metal ions to promote their uniform distribution on the support and inhibit aggregation.[54,55] For example, Ru SAs supported on CNFs have been synthesized by integrating electrospinning with the NH_3-assisted synthetic route.[56] This methodology leverages the synergistic reduction and coordination effects of NH_3, facilitating the efficient dispersion and stabilization of metal SAs. Such catalysts demonstrate extensive utility across diverse catalytic reactions. Similarly, Wang *et al.* demonstrate the fabrication of Fe SACs through pyrolysis of Fe^{3+}-containing polyvinylidene fluoride (PVDF) nanofiber membranes under an NH_3 atmosphere.[57] The resulting Fe species exist as isolated SAs stabilized within an Fe–N_4–C configuration.

3.2 Thermodynamically driven atomic migration approach

SAs can be thermally migrated *via* high-temperature treatment, with their immobilization markedly boosting the catalyst performance. The phenomenon whereby larger particles engulf smaller ones is known as Ostwald ripening.[58] For instance, high-

temperature treatment of the powdered CeO_2 substrate effectively traps Pt species, yielding sintering-resistant catalysts with uniformly distributed active sites.[59] Recent work demonstrates a novel strategy for stabilizing Ni atoms on robust vanadium carbide (VC) coupled with NCNFs through a thermodynamically driven dynamic atomic migration process.[60] A thermal gradient facilitates the direct atomization of Ni NPs into SAs, which are subsequently captured and densely dispersed across NCNFs *via* strong metal–support interactions (Fig. 3a). Given the superior adsorption energy of VC for Ni atoms over carbon, the unbound Ni atoms spontaneously migrate from Ni NPs to VC integrated within the NCNFs. This process yields a stable Ni SA-VC

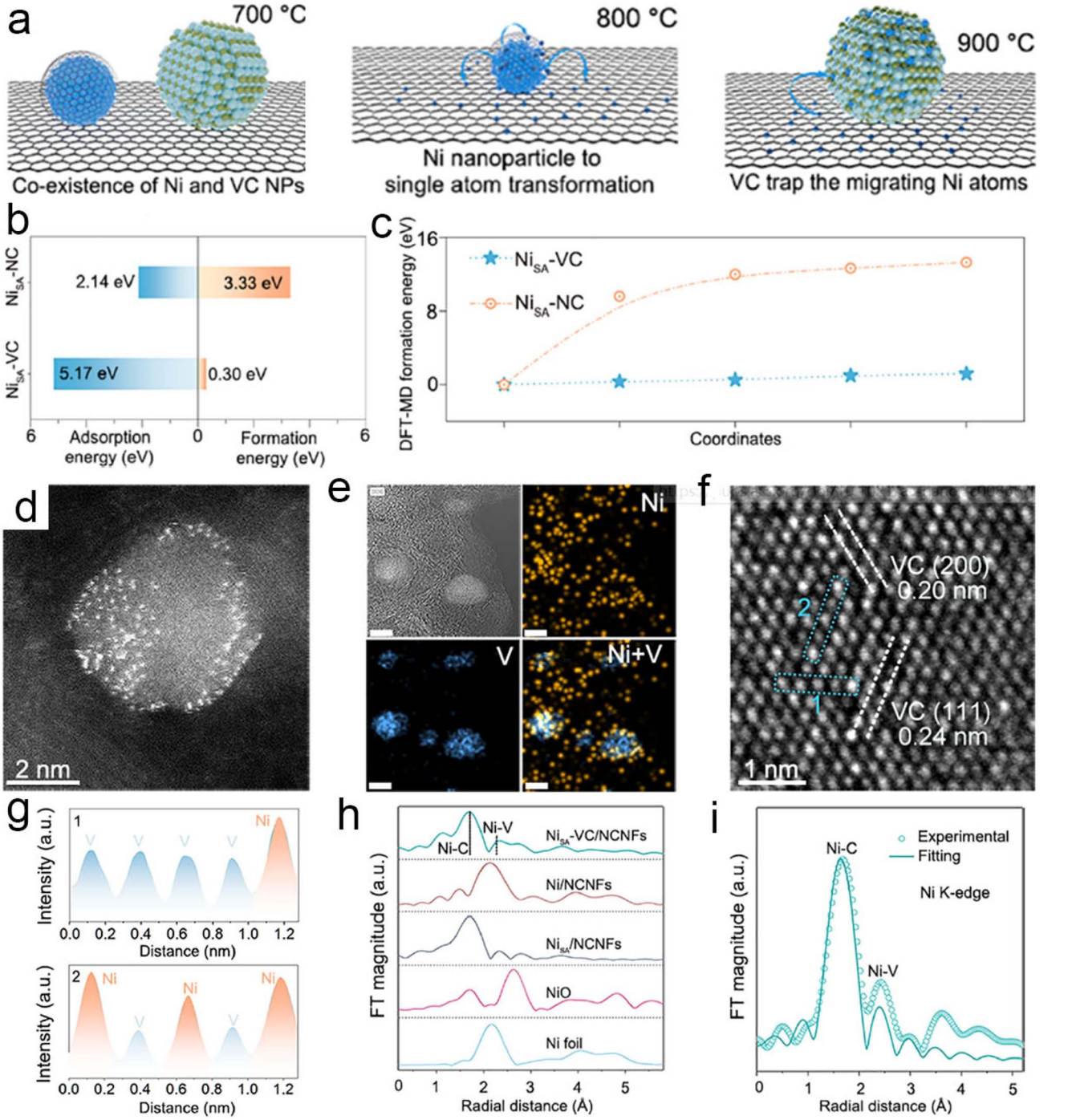

Fig. 3 (a) Illustrative models of the progression of Ni SA-VC under thermal gradient conditions. (b) The formation energies for Ni SA-NC and Ni SA-VC structures and Ni atom adsorption energies on NC and VC supports *via* the DFT route. (c) Thermodynamic formation energy of Ni SA on NC and VC supports *via* DFT-MD simulations. (d) HAADF-STEM image of Ni SA-VC hosted on NCNFs. (e) STEM-EDS compositional images of Ni SA-VC/NCNFs; scale bar: 5 nm. (f) HRTEM image of Ni SA-VC and (g) extracted intensity profiles. (h) Ni K-edge FT-EXAFS spectra of varied samples. (i) Fitting curve of the Ni K-edge of N SA-VC/NCNFs. Reproduced with permission.[60] Copyright 2023, American Chemical Society.

architecture with minimized formation energy. Density functional theory (DFT) calculations reveal that the adsorption energy of VC (5.17 eV) exceeds that of NCNF (2.14 eV) (Fig. 3b). Additionally, the formation energy (E_f) for Ni SA on VC (0.30 eV) is lower than that on NC (3.33 eV). These findings suggest that the Ni SA-VC structure is thermodynamically more stable than the Ni SA-NCNF configuration. This is also corroborated by the lower DFT-molecular dynamics (DFT-MD) formation energy (Fig. 3c). HAADF-STEM, energy-dispersive X-ray spectroscopy (EDS), high-resolution transmission electron microscopy (HRTEM), and EXAFS results confirm the formation of Ni SAs on the VC matrix (Fig. 3d–i).

3.3 Wet-impregnation method

The conventional impregnation protocol involves submerging a prepared nanofiber film into a solution containing the target element. Following a designated period, atoms deposit onto the surface of the nanofiber, subsequent to which the material harboring these atoms is subjected to washing and drying. As previously discussed, MOFs facilitate SA generation within a carbon matrix during pyrolysis. Significantly, MOF-derived N-doped carbon can directly serve as the SA support. Typically, NPCNFs that are fabricated from the carbonization of PAN/ZIF-8 nanofibers display an amorphous macro-porous structure (Fig. 4a and b), providing an effective scaffold for immobilizing Pt SAs *via* adsorption and heat treatment.[30] The AC HAADF-STEM and elemental mappings reveal the uniform distribution of Pt SAs within NPCNFs (Fig. 4c–e). X-ray absorption near-edge structure (XANES), wavelet transform and EXAFS fitting analysis confirm the formation of Pt SAs with a Pt–N_2C_2 coordination configuration (Fig. 4f–j), attributed to the trapping effect of the rich porous architecture and the nitrogen functionalities present in the NPCNFs. The pronounced electronegativity contrast between Pt atoms and the adjacent N/C atoms induces substantial electron perturbation, altering the electronic state of Pt centers.

3.4 Electric field-confined strategy

A novel electric field-confined SA seeding strategy has recently been proposed for preparing SACs.[61] This approach utilizes a dual electrospinning–electrospraying synthetic route, followed by thermal treatment to produce Ti SAs and sub-3 nm clusters within a 3D porous network (Fig. 5a). Specifically, PAN serves as the primary electrospinning material, while titanium butoxide (TBT) is incorporated into the electrospraying solution. Under the potent electric field, TBT is intensively

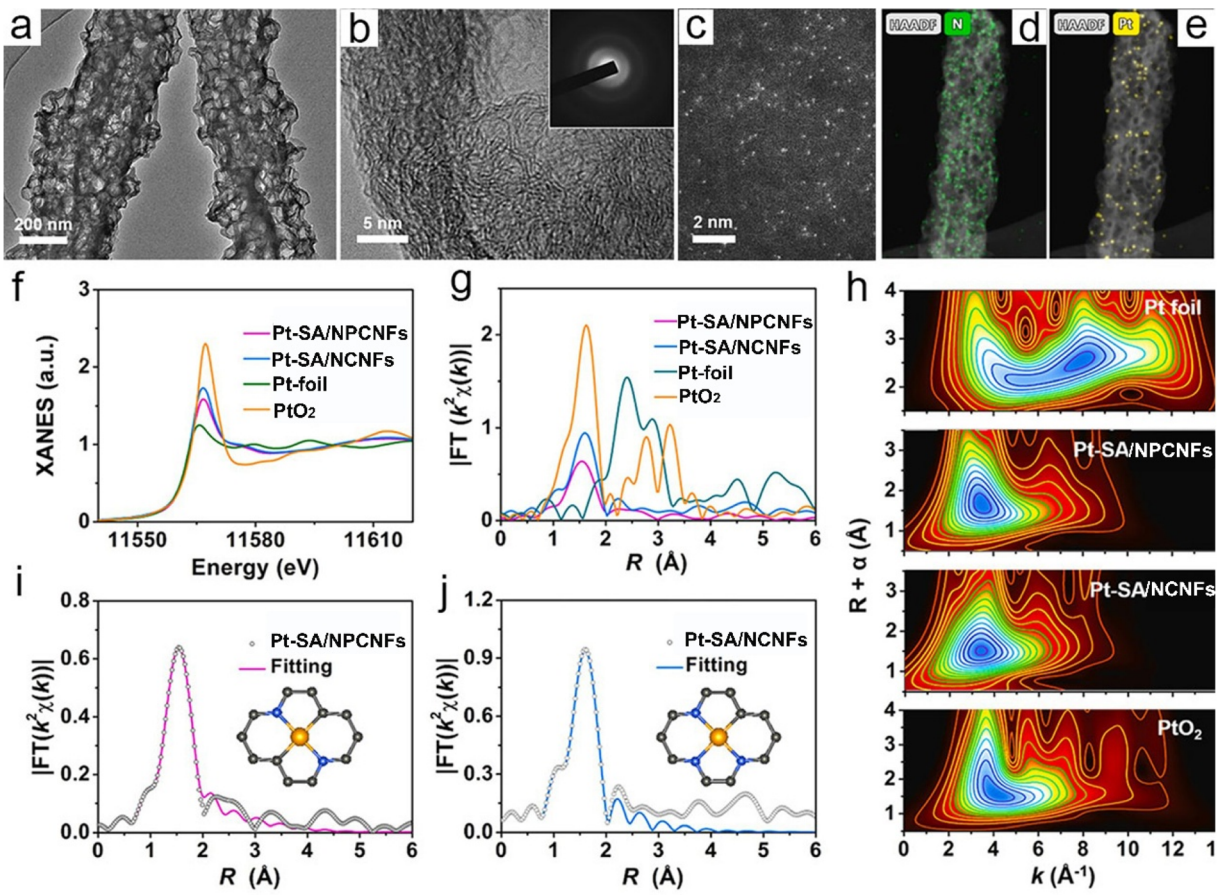

Fig. 4 (a) TEM image, (b) HRTEM image with a selected area electron diffraction (SAED) pattern, (c) AC HAADF-STEM image, and EDX elemental mapping of (d) N and (e) Pt. (f) L3-edge XANES and (g) FT EXAFS spectra of varied samples. (h) Wavelet transform study. (i) Pt L3-edge EXAFS and (j) EXAFS fitting curves of the Pt SA-based catalyst. Reproduced with permission.[30] Copyright 2023, Elsevier.

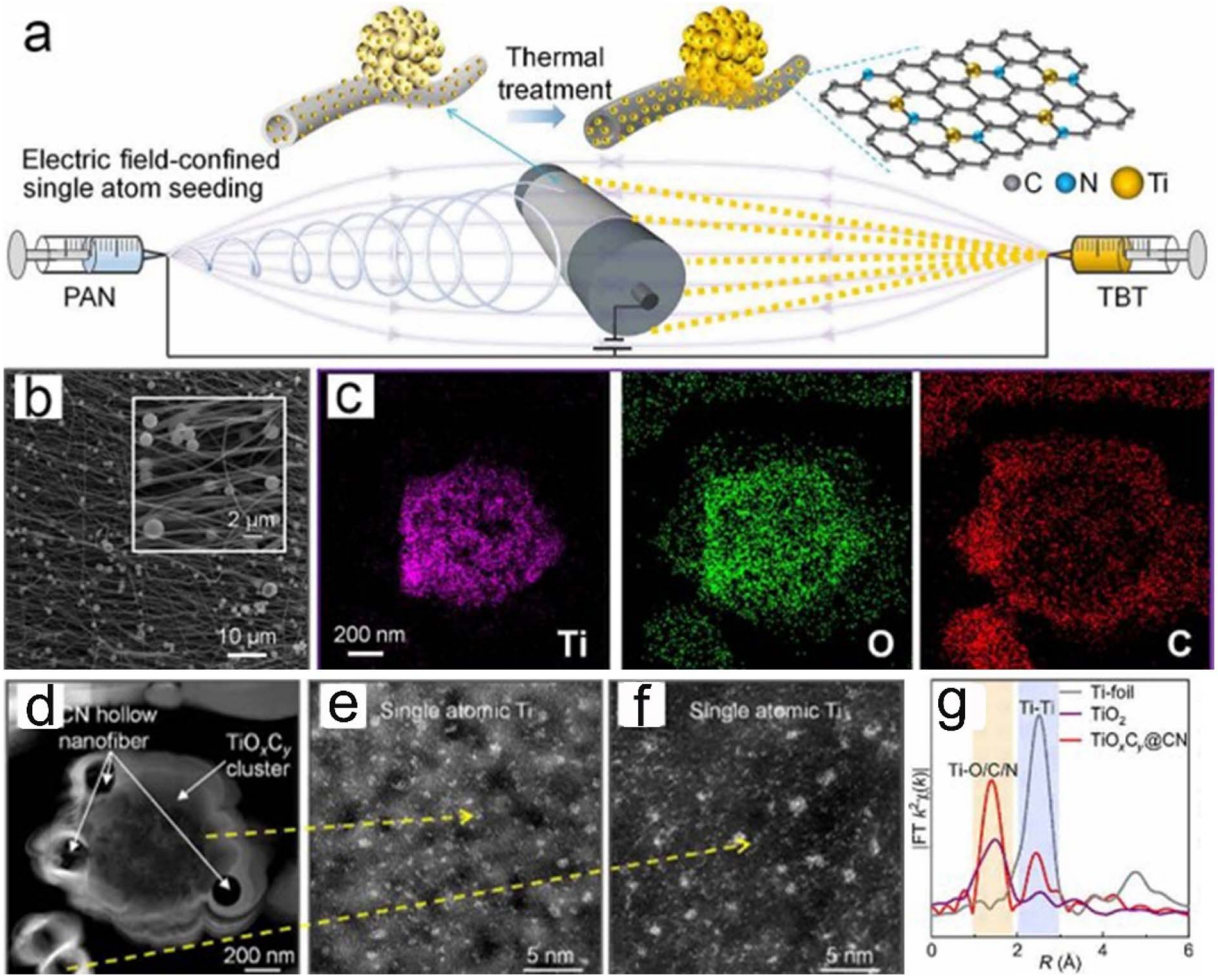

Fig. 5 (a) Schematic illustration of the dual electrospinning–electrospraying fabrication strategy *via* electric field-confined SA seeding. (b and c) SEM image and elemental mapping of the TiO_xC_y clusters with the carbon matrix. (d) Zoomed-in STEM image of the TiO_xC_y clusters with the carbon matrix. (e and f) AC HAADF-STEM image of the TiO_xC_y clusters with Ti SAs. (g) Comparative EXAFS spectra of synthesized samples. Reproduced with permission.[61] Copyright 2025, American Association for the Advancement of Science.

fragmented and highly dispersed as clusters or individual molecules into the PAN matrix. Concurrent cross-linking reactions likely facilitate the formation of strong chemical bonds between TBT and PAN. The simultaneous and continuous electrospinning–electrospraying process ensures inherent 3D structural connectivity (Fig. 5b). AC-HAADF-STEM reveals that the resultant Ti SAs and TiO_xC_y clusters originate from TBT molecule seeds confined within the as-spun and pre-oxidized samples by the electric field effect. Further thermal treatment converts these confined TBT seeds into Ti SAs and sub-3-nm TiO_xC_y clusters, which become fused with the carbon matrix (Fig. 5c–f). Notably, the Ti SAs distribute not only proximal to TiO_xC_y clusters but also within the hollow carbon fibers, distant from these clusters. EXAFS analysis further reveals that the Ti valence state in the TiO_xC_y@CN membrane is notably sub-tetravalent (Fig. 5g).

3.5 Microwave heating-assisted strategy

Microwave heating has recently been highlighted as an advanced thermal processing technique for materials fabrication, where its rapid and uniform energy delivery kinetically suppresses metal atom migration and agglomeration during SAC synthesis. In a typical example, atomically dispersed transition metals (TM = Fe, Co, Ni, FeCo, FeNi) on NPCNFs have been constructed *via* electrospinning coupled with controllable microwave processing.[62] A pivotal feature of this methodology involves incorporating carbon black microwave absorbers within ENFs, which exhibits a remarkably ultrafast heating rate of ~200 °C min^{-1} under microwaves, achieving up to 97.5% reduction in energy consumption (Fig. 6a–c). This rapid thermal profile significantly suppresses random metal atom migration and aggregation compared to traditional thermal methods that favor bulk nanoparticle formation (T–Fe/NPCNFs-900) (Fig. 6d–f). Consequently, a typical M–Fe/NPCNFs-900 catalyst synthesized from the microwave heating method with highly exposed atomic Fe–N_4 sites is successfully synthesized (Fig. 6g–m). This study establishes a generalizable pathway for rapid fabrication of high-performance SACs on NPCNFs for advanced energy conversion and storage systems.

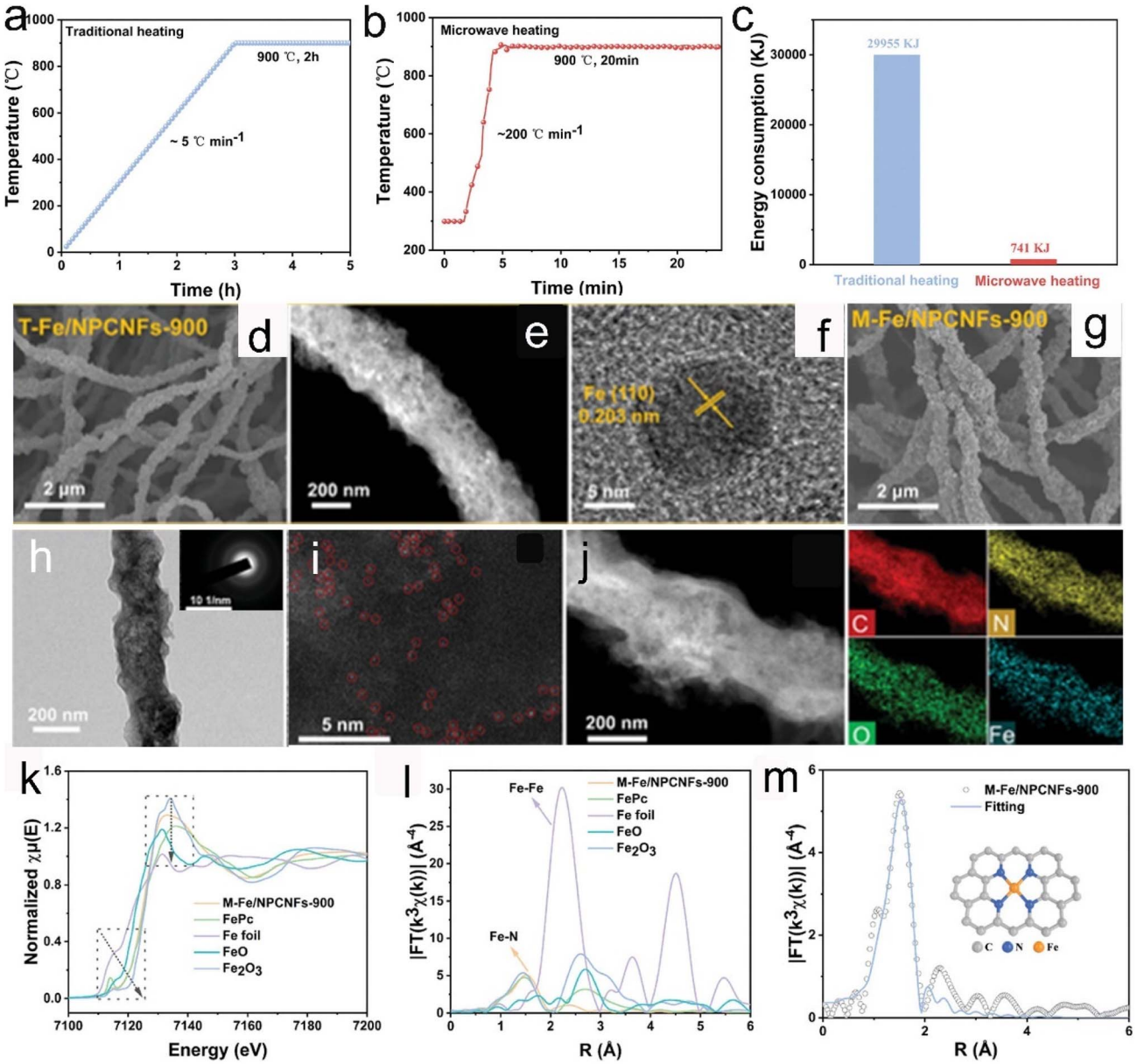

Fig. 6 (a and b) Temperature profiles to prepare Fe/NPCNFs-900 catalysts under traditional and microwave heating. (c) Total energy consumption comparison for traditional and microwave heating methods. (d) SEM, (e) HAADF-STEM, and (f) HRTEM images of T–Fe/NPCNFs-900. (g) SEM, (h) TEM, (i) AC HAADF-STEM, and (j) HAADF-STEM images with elemental mapping for C, N, O, and Fe of M–Fe/NPCNFs-900. (k) XANES and (l) FT EXAFS spectra of varied samples. (m) EXAFS fitting curves of the M–Fe/NPCNFs-900 catalyst. Reproduced with permission.[62] Copyright 2024, John Wiley and Sons.

4. Characterization and theoretical calculations

The integration of SACs with electrospinning technology has significantly broadened their application scope. To gain in-depth insights into their morphological and structural characteristics, it is imperative to employ advanced characterization techniques capable of analyzing the interactions between SAs and support matrices. The combined approach of HAADF-STEM imaging and X-ray absorption fine structure (XAFS) spectroscopy provides a powerful analytical tool for identifying the presence and distribution of specific elements through atomic-resolution analysis.[63,64] Furthermore, computational methods based on DFT can further elucidate the interaction mechanisms between SAs and supports, clarifying the underlying principle of the exceptional catalytic performance. This dedicated section will comprehensively outline advanced characterization techniques and theoretical computational methods used for SA structural analysis, revealing the mechanisms responsible for the high performance of SACs.

4.1 AC HAADF-STEM

AC-HAADF-STEM has now become the most effective and intuitive characterization technique for identifying SA sites. Compared to conventional HRTEM, it provides atomic-level fine

structure details of catalysts. In AC-HAADF-STEM images, small bright spots with several angstroms in size typically correspond to individual atoms. The imaging intensity of these atoms is proportional to the square of the atomic number. This enables straightforward differentiation between heavy metal atoms (*e.g.*, Fe, Co, Ni, and Pt) and light atoms (*e.g.*, C, N, and S), thereby revealing the coordination environment between metal atoms and non-metal atoms within the support. Furthermore, AC-HAADF-STEM can be combined with techniques such as SAED and EDS to provide detailed information on the crystallographic properties, composition, elemental distribution and content of the electrocatalyst. For instance, HRTEM clearly reveals distinct lattice fringes corresponding to Fe nanoparticles in the T–Fe/NPCNF catalyst (Fig. 6f). However, SAED patterns of the M–Fe/NPCNF catalyst show only diffuse rings from carbon (Fig. 6h). Further analysis *via* AC-HAADF-STEM identifies the corresponding high-intensity bright spots as Fe SAs (Fig. 6i). Additionally, this technique can characterize the distribution of diatomic sites within ENF structures. For example, in the CuNi-diatomic-ENF catalyst, adjacent Cu and Ni atoms spaced approximately 0.24 nm apart are clearly resolved.[65] This spatial distribution corresponds well with the elemental maps obtained from EDS results.

4.2 XAFS

XAFS spectroscopy is a highly sensitive analytical technique for probing elemental composition, coordination structures, and chemical states of materials. By detecting changes in X-ray absorption characteristics before and after irradiation, XAFS investigates the electronic states and microscopic structures of samples, playing an indispensable role in assessing the distribution of SA sites on the support and their local electronic environments, showing significant advantages compared to other analytical methods. Based on formation mechanisms and spectral profiles, XAFS comprises two regimes of XANES and EXAFS. XANES probes electronic transition characteristics near the absorption edge, resolving fine structural variations adjacent to the absorption threshold to detect subtle differences in the atomic coordination environment. This technique enables precise identification of material composition and elemental oxidation states. Complementarily, EXAFS spectroscopy analyzes high-energy oscillatory signals within 50–1000 eV

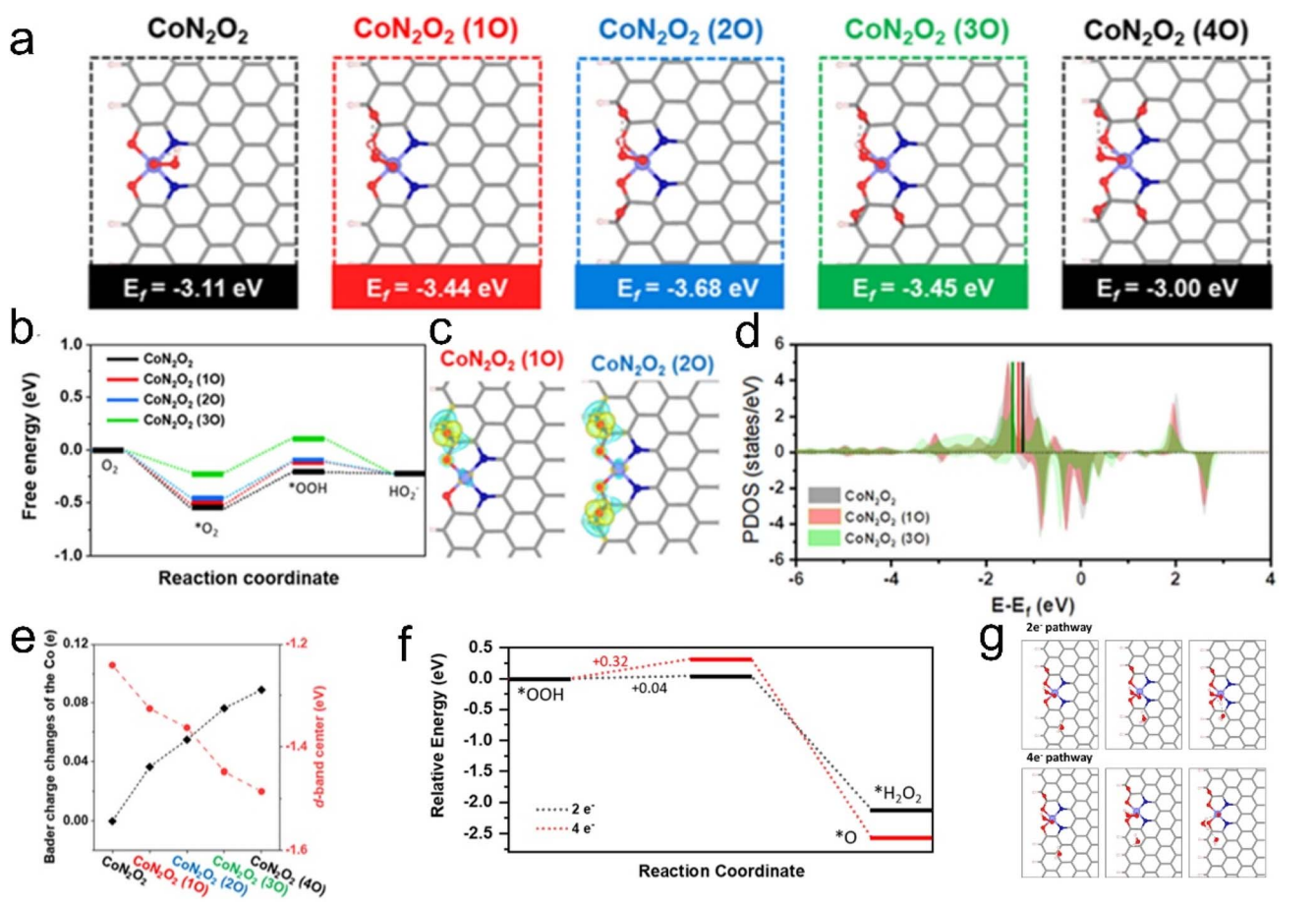

Fig. 7 (a) Optimized geometries of *OOH adsorbed on various CoN_2O_2 configurations. (b) Free-energy diagrams of the 2e$^-$ ORR on CoN_2O_2 configurations at pH 13 and 0.65 V *versus* RHE. (c) Charge density differences of CoN_2O_2 (1O) and CoN_2O_2 (2O) on graphene. (d) Projected DOS of the Co site with d-band centers for CoN_2O_2 (black), CoN_2O_2 (1O, red), and CoN_2O_2 (3O, green). (e) Epoxy oxygen coordination effects on Co Bader charge (black) and d-band center (red). (f) Energy barrier for *OOH reduction *via* 2e$^-$ and 4e$^-$ ORR pathways with (g) initial, transition, and final states configurations. Reproduced with permission.[36] Copyright 2024, John Wiley and Sons.

beyond the absorption edge, determining precise local atomic configurations around absorbed atoms, including critical parameters such as interatomic distances and coordination numbers. EXAFS employs Fourier transform techniques to construct short-range ordered structural models, with experimental data fitting procedures extracting quantitative structural parameters. As depicted in Fig. 6k, the Fe K-edge absorption energy of M–Fe/NPCNFs-900 resides between those of FeO and Fe_2O_3, indicating an iron valence state between +2 and +3. Concurrently, EXAFS (Fig. 6l) exhibits a characteristic Fe–N peak at 1.5 Å with no detectable Fe–Fe coordination peak at 2.2 Å, confirming the formation of Fe single atoms (Fe SAs). Further refinement *via* FT-EXAFS fitting (Fig. 6m) resolves the atomic-scale Fe–N_4 coordination structure.

4.3 DFT

DFT provides a powerful computational framework for investigating active sites and reaction mechanisms in SACs.[66,67] When integrated with experimental characterization studies, DFT enables more efficient exploration of electrocatalytic processes. General analytical methods include the Bader charge analysis for probing charge distribution and bonding environments at active sites, charge density difference to visualize electron transfer during catalysis, electron localization function (ELF) for determining chemical bond types, density of states (DOS) studies of orbital interactions, crystal orbital Hamilton population (COHP) for bond strength analysis, transition state theory (TST) calculations of reaction energy barriers.[34,42,68–73] As exemplified by the Co-SAC system anchored on electrochemically surface-treated aligned CNFs, Hwang *et al.* employed DFT to calculate the formation energies of all feasible CoN_xO_y configurations and Co binding energies, determining the atomic structure.[36] The epoxy-functionalized CoN_2O_2(1O) and CoN_2O_2(2O) configurations show excellent agreement with EXAFS analysis (Fig. 7a). Fig. 7b demonstrates decreasing adsorption energy with increasing epoxy oxygen coordination. Charge density difference calculations reveal electron depletion at the Co SA center and charge accumulation around the epoxy O atoms (Fig. 7c and d), which is also consistent with Bader charge analysis (Fig. 7e). The electron-withdrawing effect causes the downward shift of the Co d-band center, weakening adsorbate interaction (Fig. 7f and g). The energy barrier calculation for CoN_2O_2 indicates that the $2e^-$ ORR pathway to H_2O_2 is kinetically favored over the thermodynamically preferred $4e^-$ pathway to H_2O. This preference arises primarily due to the significantly lower energy barrier for *OOH conversion to H_2O_2 compared to *O dissociation, confirming superior reaction kinetics for the $2e^-$ ORR pathway.

5. Potential applications for energy catalysis

SA-ENFs demonstrate exceptional electrocatalytic efficacy, which is ascribed to the homogeneous distribution of catalytic centers and the high atomic utilization efficiency. Furthermore, the modification of the local electronic structure upon the integration of additional atoms results in an increased exposure of active sites. The one-dimensional (1D) nanoarchitecture effectively facilitates electron and mass transfer dynamics, collectively contributing to the enhancement of the electrocatalytic performance.

5.1 HER

Hydrogen (H_2) serves as a green, renewable, and eco-friendly energy carrier, substantially mitigating reliance on fossil fuels.[74–80] Electrochemical water splitting, effectively driven by alternative energy sources, provides a route for H_2 generation.[81] As a cathodic half-reaction, the HER encompasses the H intermediate (H*) adsorption on the electrocatalyst in common electrolytes and requires water dissociation in alkaline environments. This process typically necessitates efficient electrocatalysts. While precious metal-based nanomaterials represent the benchmark HER catalysts, their scarcity and high cost substantially limit their potential for widespread commercial adoption. The advancement of SACs offers a pivotal opportunity to not only boost the HER efficiency but also achieve a more cost-effective solution.[30,34,35,54,82] Notably, integrating a SA within NCNFs establishes unique interactions with N atoms, optimizing the electronic structure and thereby enhancing the electrocatalytic activity.

As a prototypical illustration, Fe SAs have been successfully embedded within porous NCNFs, establishing a coordination structure between the Fe and N atoms. EXAFS analysis reveals an average Fe–N bond length of 2.02 Å, confirming the formation of an Fe–N_5 coordination environment. The obtained electrocatalyst demonstrates excellent performance for acidic/alkaline-universal HER operation.[83] In 0.5 M H_2SO_4, the optimized Fe-SA-based catalyst shows a lower overpotential of 44.3 mV at 10 mA cm^{-2} (η_{10}) and a Tafel slope of 45.4 mV dec^{-1}, outperforming its Fe-NP-based counterparts (76.0 mV and 55.1 mV dec^{-1}). The superiority is further evidenced by a turnover frequency (TOF) of the Fe-SA-based catalyst (0.72 s^{-1}), which is 4.5-fold higher than that of the Fe-NP-based catalyst, signifying its enhanced intrinsic acidic HER activity. The exceptional HER activity correlates with rapid charge transfer capability and abundant accessible electrochemical active sites. The electrocatalyst also presents robust durability, maintaining activity with minimal current density loss after 2000 CV cycles. In 1 M KOH solution, the electrocatalyst exhibits commendable HER activity, though slightly reduced compared to the acidic environment.

Ruthenium (Ru) has recently emerged as a promising Pt alternative due to its comparable H* binding affinity and superior economic viability. Consequently, Ru SAs incorporated into NCNFs are synthesized for the HER.[56] The obtained optimized Ru SA-based catalyst demonstrates a mass activity of approximately 390 A g^{-1} at an overpotential of 100 mV, which is 3.5-fold higher than that of a commercial Pt/C catalyst (110 A g^{-1} Pt). The Tafel slope of the electrocatalyst (71 mV) at 20 mA cm^{-1} is significantly lower than that of the Pt/C catalyst (171 mV $decade^{-1}$). The enhanced HER activity of the Ru SA-based catalyst is attributed to its greater number of

Table 1 Summary of HER and OER performance of typical SA-ENF catalysts

Catalysts	Electrolyte	j (mA cm^{-2})	η (mV)	Tafel slope (mV dec^{-1})	Stability (h)	Coordination motifs	Reference
Pt-SA/pCNFs for HER	0.5 M H_2SO_4	10	21	24	200 (at 10 mA cm^{-2})	Pt–N_2C_2	30
		500	43				
Ni SA/NP-NCF-800 for HER	1 M KOH	10	137.3	157	27 (at 10 mA cm^{-2})	Ni–N_4	34
Mo@NMCNFs for HER	0.5 M H_2SO_4	10	66	48.9	16.67 (at 66 mV)	Mo–$O_1N_1C_2$	35
V@NMCNFs for OER	0.5 M H_2SO_4	10	196	25	60 (at 20, 40, and 60 mA cm^{-2})	V–O_2N_3	50
a-Ru@Co-DHC for HER	1 M KOH	10	40	62	10 (at 10 mA cm^{-2})	—	54
Ru SAs/NCNF-800-1 for HER	1 M KOH	20	34	71	20 (at 20 mV)	—	56
MCM@MoS_2–Ni for HER	0.5 M H_2SO_4	10	161	81	24 (at 250 mV)	—	82
Rh–TiO_2/CNF for HER	1 M KOH	10	24	24.5	52.5 (at 100 mA cm^{-2}) + 60 (at 200 mA cm^{-2})	—	84
Fe–N–C-300/Fe NP for OER	1 M KOH	10	263	40.67	48 (at 10 mA cm^{-2})	—	90
		100	305				
Ni–N,P/CNFs for OER	1 M KOH	10	330	65	—	Ni–N_3–P	133
Ni–N,P/CNFs for HER	1 M KOH	10	84	126			
		50	272				
	0.5 M H_2SO_4	10	38	24			
		100	94				
Ir^{SA}–Ir^{NC12}-NiMn-LDH-F for OER	1 M KOH	10	249	—	60 (at 10 mA cm^{-2})	—	134
Ir^{SA}–Ir^{NC12}-NiMn-LDH-F for HER	1 M KOH	10	110	—	50 (at 10 mA cm^{-2})		

electrochemical active sites and efficient electron transfer. The catalyst also presents robust stability, maintaining performance with only minimal current density degradation after 20 hours of continuous operation. Recently, a Rh SA catalyst has been reported, demonstrating efficient alkaline HER activity due to the synergistic effect of dual active sites (Rh–N_x and Rh–O_x).[84] When fabricated into the cathode of an anion exchange membrane water electrolyzer (AEMWE), the single-cell exhibits an exceptional current density of 953 mA cm^{-2} at 2.2 V, significantly outperforming the Pt/C catalyst while maintaining excellent durability. Notably, recent studies confirm that SA-ENFs universally exhibit high HER activity and durability (Table 1).

5.2 OER

The OER, serving as the anodic half-reaction in water electrolysis, encompasses a complex four-proton/four-electron transfer mechanism. This inherent complexity poses a significant challenge, often constituting a bottleneck in the overall water splitting process. Consequently, enhancing OER catalytic efficiency is crucial for boosting the performance of water decomposition systems.[85–90] In the realm of catalyzing the OER, SA-ENFs have also emerged to present exceptional performance.

While many reported transition SA catalysts utilize N-functionalized carbon supports, their efficacy is often limited by high structural/electronic symmetry and chemical inertness. Introducing non-metal heteroatoms to modulate coordination environments and disrupt symmetry represents a promising strategy for enhancing electrocatalytic activity. Notably, the O atoms possessing higher electronegativity than N atoms can distort the metal–N parallelogram structure when incorporated. This distortion strengthens electronic metal–support interactions, lowers activation energy barrier for the rate-determining step (RDS), and ultimately boosts electrocatalytic activity. Among the array of 3d transition metals, vanadium (V) exhibits exceptional promise as a non-noble electrocatalyst due to its multivalent nature, abundance of unoccupied d-orbitals, and robust redox properties. Inspired by this, the V SA catalyst supported on NMCNFs was successfully achieved through a SiO_2-assisted electrospinning–pyrolysis–etching process for OER application.[50] This catalyst features open mesoporous channels, facilitating rapid access of reactant molecules to active sites and promoting the release of gaseous products. This significantly enhances the intrinsic activity of the OER. Consequently, the obtained electrocatalyst exhibits exceptional acidic OER activity, with a η_{10} of 196 mV and a Tafel slope of 25 mV dec^{-1}, outperforming many benchmarks (Fig. 8a–d). The V SA-based catalyst also exhibits a higher C_{dl} value than VO-based catalysts, demonstrating its larger electrochemical active area (Fig. 8e). Critically, vanadium adopts a five-coordinated O-axial VO_2N_3 configuration within the NMCNFs, which optimizes its electronic structure, reduces the free energy barrier for the OH* to O* transition, and further enhances the OER kinetics (Fig. 8f–h). Recent studies confirm that SA-ENF catalysts incorporating V, Ni, and Ir universally deliver high OER activity and stability (Table 1).

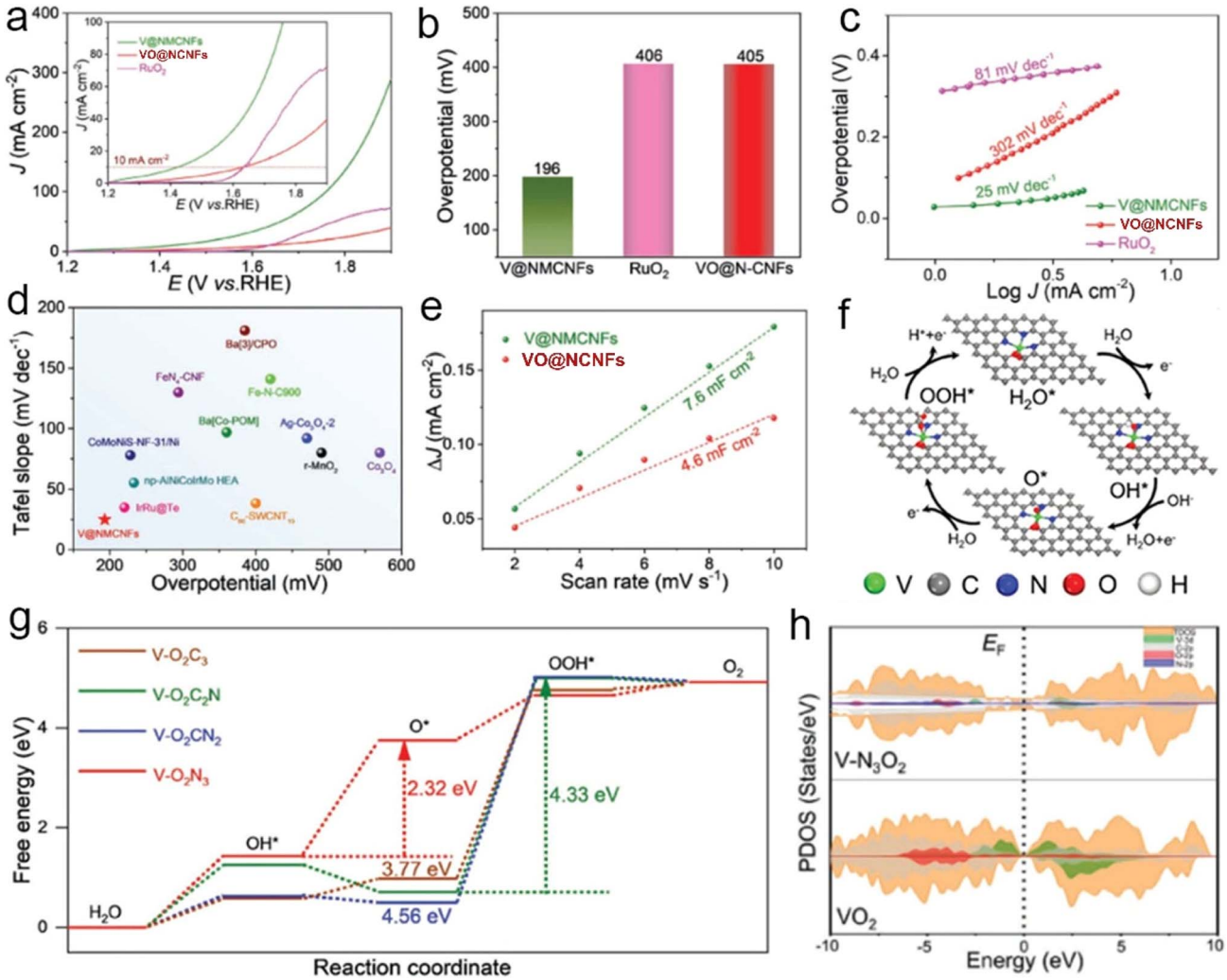

Fig. 8 (a) LSV plots, (b) the overpotentials at 10 mA cm^{-2}, and (c) Tafel plots of varied catalysts in 0.5 M H_2SO_4. (d) Comparisons of OER activity with reported catalysts. (e) C_{dl} analysis of V@NMCNFs and VO@NCNFs. (f) OER pathway evaluation on V-SAs. (g) Gibbs free-energy profiles of the OER pathway on varied catalysts. (h) The projected DOS (PDOS) of V–O_2N_3 and VO_2 structures. Reproduced with permission.[50] Copyright 2022, John Wiley and Sons.

5.3 ORR

Fuel cells and metal–air batteries represent prominent energy conversion technologies due to their minimal environmental impact and high energy conversion efficiency. The ORR at the cathode is central to their operation. While Pt-based catalysts have traditionally demonstrated superior catalytic efficiency, their prohibitive cost and limited durability pose substantial challenges for long-term deployment, thereby constraining the broader application of these energy devices.[91–95] Recent research has identified the M–N_4 moiety as the primary active site for the ORR within the diverse M–N–C electrocatalysts, establishing it as a cutting-edge research frontier.[96] Hence, the design of SA-ENFs emerges as a critical strategy to enhance the ORR performance.[62,97]

Architecture control is paramount for achieving high electrocatalytic performance in the ORR. The 3D carbonaceous skeleton, for instance, typically offers excellent electrical conductivity and mass transfer capabilities, enabling superior ORR properties. The electrospinning technique provides a direct route to construct a self-supporting 3D nanofibrous structure that effectively anchors SACs for the ORR. A representative approach involves incorporating hemin with its chloroprotoporphyrin IX iron(III) structure into electrospun PAN nanofibers, followed by peroxidation and pyrolysis to yield a self-standing nanofibrous Fe–N-CNF membrane as an ORR electrocatalyst.[37] EXAFS analysis of the optimized Fe–N-CNFs reveals a mean first-shell coordination number of four, verifying the formation of catalytically active Fe–N_4 moieties instrumental in enhancing ORR performance. Notably, in alkaline electrolyte, this catalyst exhibits an onset potential (E_{onset} = 0.94 V *vs.* RHE) and half-wave potential ($E_{1/2}$ = 0.84 V), surpassing those of Pt/C (0.89 V and 0.79 V, respectively), operating primarily *via* a four-electron transfer pathway. Furthermore, the stability testing over a period of 12 000 seconds reveals a higher retention rate for the Fe–N-CNF catalyst (88.6%) compared to Pt/C (84.7%), highlighting its superior

durability, while also exhibiting commendable ORR activity under acidic conditions. Similarly, copper (Cu)–N-CNFs featuring a Cu–N_4 configuration have also been successfully prepared by pyrolyzing sodium copper chlorophyllin within PAN nanofibers, resulting in a catalyst possessing an ultra-high specific surface area and superior electron/mass transfer capabilities. Consequently, this catalyst outperforms commercial Pt/C in both catalytic activity and stability under alkaline media.[98]

Unlike the four-electron ($4e^-$) ORR, which produces water, the two-electron ($2e^-$) pathway generates H_2O_2. This dual functionality enables it to serve as not only a cathode reaction in energy conversion devices but also a method for producing valuable chemical feedstocks. Electrochemical H_2O_2 synthesis *via* the $2e^-$ ORR offers compelling advantages for on-site production, including cost-effectiveness, enhanced safety, environmental compatibility, and high yield. Recently, SA-ENFs have emerged as a highly promising electrocatalyst platform for the $2e^-$ ORR pathway, demonstrating exceptional performance in selective H_2O_2 production.[99] Hwang *et al.* also demonstrated that the Co-based SA-ENF catalyst exhibits excellent $2e^-$ ORR activity, achieving a high H_2O_2 yield rate of 15.75 mol g_{cat}^{-1} h^{-1} at 300 mA cm^{-2}. Experimental characterization and theoretical calculations confirm that this enhanced ORR activity and selectivity originate from atomically dispersed Co sites anchored at defect-rich edges of the carbon carrier, featuring Co–N_2–O_2 coordination motifs and electron-withdrawing epoxy oxygen groups.[36] Table 2 summarizes the ORR performance of some typical SA-ENF catalysts for both $4e^-$ and $2e^-$ pathways (Table 2).

5.4 HOR

The hydrogen oxidation reaction (HOR) constitutes a fundamental electrochemical process in proton exchange membrane fuel cells (PEMFCs), which usually utilize Pt-based materials as the benchmark electrocatalysts. However, they face a critical operational challenge with a sensitivity to CO poisoning. Even trace amounts of CO exhibit strong adsorption affinity for Pt surfaces, impeding H_2 adsorption and subsequent dissociation, leading to a substantial deterioration in HOR efficiency. Consequently, improving CO tolerance is a critical requirement for advancing the commercial feasibility of PEMFCs.

Recently, a CO-tolerant HOR electrocatalyst composed of NCNF decorated with atomically dispersed tungsten (W) sites and Pt NPs has been developed.[100] XANES analysis reveals oxidation states of +0.97 for Pt and +2.99 for W in the obtained Pt/W@NCNF catalyst. FT-EXAFS spectra further demonstrate the coexistence of Pt–Pt and Pt–N/O coordination peaks for Pt, while only W–N/O configuration is observed for W, confirming the presence of both Pt NPs and atomically dispersed W sites. In this system, electron transfer from Pt to W optimizes the electronic configuration of Pt-5d orbitals. This enhances the adsorption behavior of varied intermediates, facilitating the HOR process. The correlation between the limiting current density and the square root of rotation rate indicates a $2e^-$ ORR HOR pathway. Remarkably, Pt/W@NCNF exhibits a mass activity of 20.6 times higher and a turnover frequency (TOF) of 24.1 times greater than those of commercial Pt/C. The catalyst also demonstrates exceptional CO tolerance, with only a 3.4% decline in current density after 20 000 cycles in H_2 containing

Table 2 Summary of ORR performance of typical SA-ENF catalysts

Catalysts	E_{onset}/V (*vs.*RHE)	$E_{1/2}$/V (*vs.* RHE)	Stability (h)	Coordination motifs	Main pathways ($4e^-$/$2e^-$)	Reference
Fe/SNCFs-NH_3	—	0.89	10 (at 1600 rpm)	Fe–N_4/C	$4e^-$	33
Co@EO-ACNF15	—	—	48 (at 100 mA cm^{-2})	CoN_2O_2	$2e^-$	36
Fe-NCNFs	0.94	0.84	3.33 (at 1600 rpm)	Fe–N_4	$4e^-$	37
Fe SACs@PNCNFs	—	0.89	0.056 (1.396 V)	Fe–N_3P_1	$4e^-$	42
M-Fe/NPCNFs-900	—	0.88	12	Fe–N_4/C	$4e^-$	62
H-CoFe@NCNF	0.96	0.85	10 (at 0.75 V)	$Co_{5.47}N$/Fe–N_4–N	$4e^-$	68
g-C_3N_4-Co@CNT/Co–N_4/C	—	0.93	3	g-C_3N_4–Co@CNT/Co–N_4/C	$4e^-$	73
Fe-TiN/NCNFs	0.78	0.56	5.56 (at 1600 rpm)	FeN_5	$4e^-$	97
$Cu_{0.6}$-NC	0.94	0.81	5.56 (at 1600 rpm)	Cu–N_4	$4e^-$	98
Co_3O_4/Co SA/PCNFs	1.01	0.87	10	Co–N_2O_2	$2e^-$	99
Fe-SA/NCF	0.97	0.85	9.72	Fe–N_4	$4e^-$	114
Co SA@NCF/CNF	—	0.88	24 (at 0.7 V)	Co–N_4	$4e^-$	115
Co SA/NCFs	—	0.85	13.89	Co–N_4	$4e^-$	116
Fe_2O_3/FeN_x@CNF	1.1	0.93	3.89 (at 1600 rpm)	—	$4e^-$	117
Co–N-CCNFMs/C	—	0.84	6	Co–N_4	$4e^-$	118
Fe/NCNFs	—	0.87	—	Fe–N_4	$4e^-$	119
Co_{SA}Ni-NCNT/CNF	—	0.85	50	$N_{3/4}$–M_x	$4e^-$	120
FeSA@HPCF	—	0.87	16	Fe–N_4	$4e^-$	121
FeMn–N–C	1.05	0.92	—	Fe–N_4/Mn–N_4	$4e^-$	122
Fe SAC/HCNF	1.01	0.905	—	Fe–N_4	$4e^-$	123
$FeCoO_x$/Fe–N–C	0.99	0.91	—	Fe–N_4	$4e^-$	124
Zn–N_4-HPCNFs	1.02	0.88	3.33 (at 1600 rpm)	Zn–N_4	$4e^-$	125
Co,Ni-SAs/S,N-CNFs	—	0.84	—	CoN_3S_1–NiN_3S_1	$4e^-$	126
Ni-SAs/HCNFs/Co-NAs	0.99	0.89	25	Ni–N_3O_1 and Ni–N_4	$4e^-$	127

1000 ppm CO. This study proves that tailoring the electronic structure of Pt catalysts through SA design can simultaneously boost HOR performance.

5.5 CO_2RR

CO_2 is a potent greenhouse gas with a profound effect on the global climate. Consequently, the transformation of CO_2 into economically viable fuels or chemicals represents a promising solution for achieving carbon neutrality. Specifically, the application of electrochemical reduction techniques to convert CO_2 directly into valuable compounds offers distinct advantages in operational simplicity and environmental efficiency, driving exponential research growth in recent years. This process yields diverse products, including carbon monoxide, formate, hydrocarbons, and alcohols, underscoring the critical need for advanced electrocatalysts that enable high selectivity toward targeted compounds.[101,102]

SA-ENFs demonstrate remarkable advantages for the catalytic CO_2RR.[38,44–46,57,65,103–105] For example, a free-standing Ni SA/porous CNF membrane has been obtained *via* a ZIF8-assisted electrospinning–pyrolysis strategy for the CO_2RR to produce CO.[104] EXAFS analysis confirms that the local coordination environment features Ni SAs tetrahedrally coordinated by nitrogen atoms, forming Ni–N_4 active sites. This hierarchically porous architecture offers extensive CO_2 diffusion pathways, while aligned graphene domains enhance electrical conductivity. Additionally, the Ni SA/porous CNF membrane possesses desirable mechanical robustness and pliability, allowing straightforward customization into a gas diffusion electrode (GDE). Accordingly, this GDE achieves highly efficient CO_2RR,

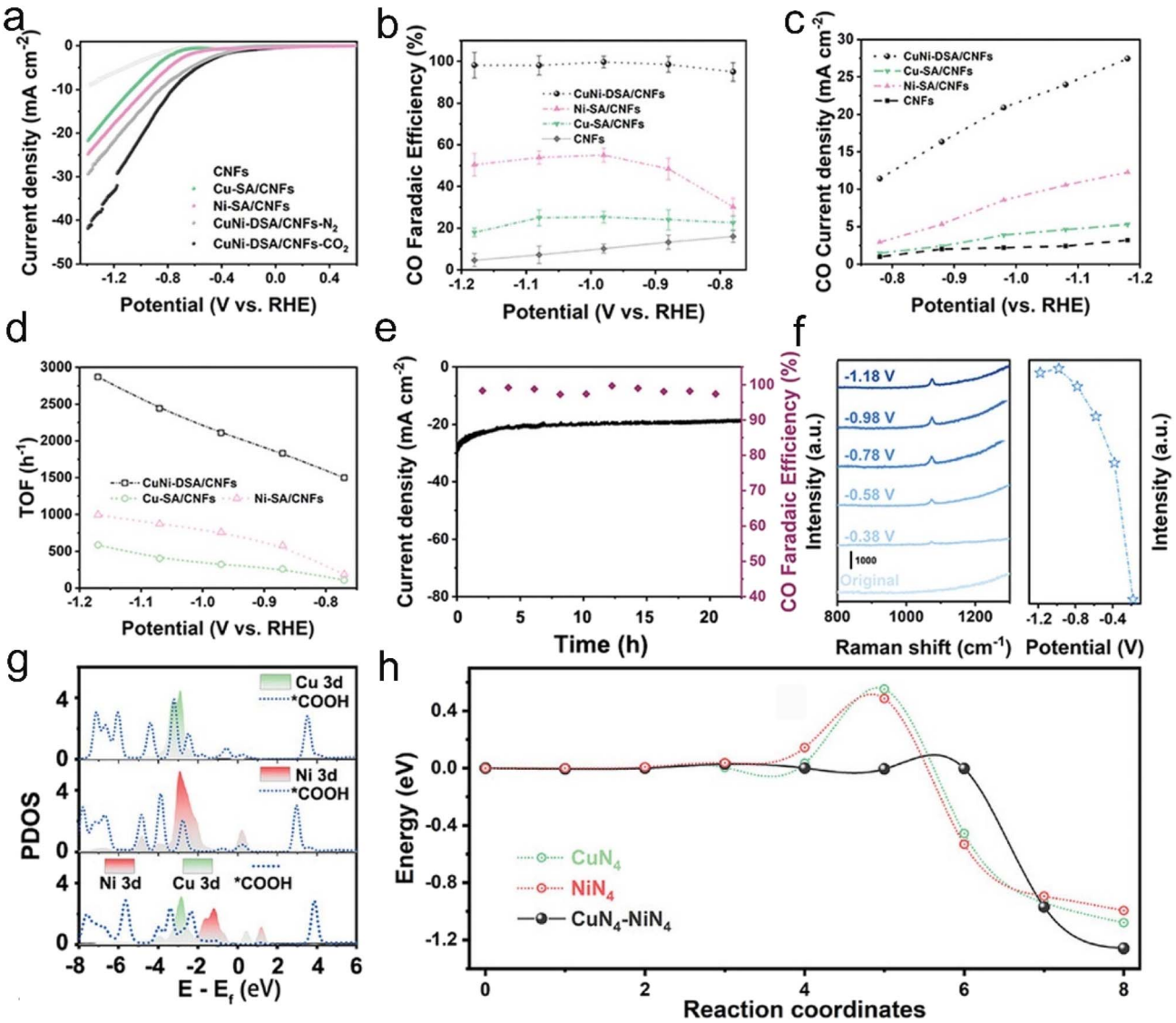

Fig. 9 (a) LSV plots of varied catalysts in CO_2-saturated 0.1 M $KHCO_3$ electrolyte. (b) FE of CO on varied catalysts. (c) Partial CO current density of varied catalysts. (d) TOFs of varied catalysts. (e) Durability measurement of CuNi DSAs/CNFs at −0.98 V *vs.* RHE. (f) *In situ* Raman spectra of CuNi DSAs/CNFs. (g) PDOS for *COOH intermediate formation on varied configurations. (h) Free energy profiles for *COOH formation on a varied coordination environment. Reproduced with permission.[65] Copyright 2022, John Wiley and Sons.

exhibiting a CO FE of 88% with a 308.4 mA cm^{-2} partial current density at −1.0 V *versus* RHE and an exceptional 120-hour operational stability. DFT analysis reveals that the RDS is the CO_2–COOH* conversion, and the free energy of this step on Ni–N_4–C (0.7 eV) is much lower than that of N–C (1.3 eV), contributing to the high performance of the production of CO from the CO_2RR. Recent studies have highlighted the promising CO_2RR performance of SACs with dual active sites.[65,106] As a typical example, a dual-site SAC (CuNi-DSA/CNFs) featuring atomically dispersed CuN_4 and NiN_4 sites on CNFs exhibits significantly enhanced CO_2RR activity compared to its single-component analogues (Fig. 9a).[65] This catalyst achieves a superior CO FE of 99.6% and a CO partial current density of −10.4 mA cm^{-2}) (Fig. 9b and c), along with a high TOF of 2870 h^{-1}, which is 4.9- and 3.4-fold higher than that of Cu-SA/CNFs and Ni-SA/CNFs, respectively (Fig. 9d). It also demonstrates a desirable durability (Fig. 9e). Raman spectroscopy reveals enhanced stabilization of *COOH intermediates on CuNi-DSA/CNFs (Fig. 9f). DFT calculations demonstrate an upshifted d-band center of CuNi-DSA (−2.36 eV) compared to Cu-SA (−3.10 eV) and Ni-SA (−2.68 eV) (Fig. 9g), which facilitates electron transfer and promotes CO_2 hydrogenation. Furthermore, the significantly lower activation energy barrier for *COOH formation on CuNi-DSA (0.08 eV) *versus* Cu-SA (0.58 eV) and Ni (0.48 eV) further confirms enhanced reaction kinetics (Fig. 9h).

The electrochemical production of alcohols from the CO_2RR holds significant value for fuels and valuable chemical feedstock applications. While copper-based electrocatalysts demonstrate superior activity for alcohol synthesis compared to their other metallic counterparts, they face challenges, including limited corrosion resistance and selectivity. Recent work has addressed these limitations through ZIF-assisted synthesis of Cu SACs featuring Cu–N_4 moieties on through-hole CNFs (TCNFs).[45] This method leverages ZIF-8 nanoparticle incorporation to generate abundant nanoholes within the structure that enhance CO_2RR performance. Consequently, the obtained Cu SA-based catalyst achieves 44% FE for methanol with a partial current density of −93 mA cm^{-2} at −0.9 V *vs.* RHE, surpassing the control samples. DFT analysis further indicates a relatively low free energy of Cu–N_4 in the RDS step of CO_2 to COOH* (1.17 eV) with positive *CO desorption energy (0.12 eV), which promotes the reduction of the *CO intermediate to methanol rather than forming CO. Recently, a Cu–Zn diatomic site catalyst embedded within CNFs has been constructed for the CO_2RR, achieving over 80% total selectivity toward alcohols.[107] In this system, Zn SAs enhance CO_2 adsorption and facilitate CO formation, while Cu SAs promote C–C coupling to yield ethanol, thus enabling superior electrocatalytic performance. Some recent typical examples of the SA-ENF catalysts for the CO_2RR with high activity and excellent stability are summarized in Table 3.

5.6 NO_3RR

NH_3 presents diverse applications as a critical industrial raw material for chemical manufacturing and as a component in hydrogen-dense materials. However, the conventional Haber–

Table 3 Summary of CO_2RR performance of typical SA-ENF catalysts

Catalysts	Electrolyte	Potential (V *vs.* RHE)	Current density (mA cm^{-2})	FE (%)	Products	Stability (h)	Coordination motifs	Reference
$K_{0.66}$–Ni-NC	0.1 M $KHCO_3$	−0.8	4	95	CO	48	—	38
Ni-PCNF-0.5PMMA	0.1 M $KHCO_3$	−1.3	7.5	98.6	CO	24 (at −1.0 V in flow-cell)/24 (at −1.0 V in H-type cell)	—	44
CuSAs/TCNFs	0.1 M $KHCO_3$	−0.9	93	44 (CH_3OH)/56 (CO)	CO and CH_3OH	50 (at −0.9 V in H-type cell)	Cu–N_4	45
Ni–N_3-NCNFs	0.5 M $KHCO_3$	−0.3	5.2	96.6	CO	120 (at −0.7 V in H-type cell)	Ni–N_3	46
Fe-NCF	0.5 M $NaHCO_3$	−0.51	5.42	97	CO	13(at −0.51 V in H-type cell)	Fe–N_4–C	57
CuNi-DSA/CNF	0.1 M $KHCO_3$	−1.4	42	90.6	CO	25 (at −0.98 V in H-type cell)	CuN_4–NiN_4	65
		−0.98	20	98	CO			
		−0.8	56.4	94	CO			
	1 M $KHCO_3$	−1.8	170	94.3	CO			
NiSA/PCFM	0.5 M $KHCO_3$	−1.0 (GDE) or −0.7 (H-type)	308.4 (GDE) or 56.1 (H-type)	88 (GDE) or 96 (H-type)	CO	120 (at −1.0 V in GDE cell)/15 (at −1.0 V in H-type cell)	Ni–N_4	104
Ni–N/IPCF@CS	CO_2-saturated solution	—	572	~100	CO	16 h > 98% (200 mA cm^{-2})	Ni–N_4	105
Fe/Se–N–C	CO_2-saturated solution	−0.45	3.3	95.6	CO	—	—	106
		−0.55	6.5	91.1				
		−1.0	272	90.7				
CuZn–CNF-1000	0.1 M $KHCO_3$	−0.3	—	61.8	EtOH	—	—	107

Bosch synthesis process is not only energy-intensive but also a significant source of carbon emissions. Consequently, the electrochemical NH_3 synthesis *via* the NO_3RR under mild conditions has garnered significant research interest in recent years.[108] This electrocatalytic conversion from NO_3^- to NH_3 presents great challenges due to intricate multi-electron transfer mechanisms, which are frequently impeded by undesirable by-product formation such as nitrite and the competing HER. The advancement of highly efficient electrocatalysts to boost NH_3 production is therefore imperative.

Recent advances have identified cost-effective transition metal-based electrocatalysts, particularly copper-based (Cu and Cu_2O) and their composites, as highly efficient materials for NO_3^--to-NH_3 conversion.[109] Recently, Co-based electrocatalysts have emerged as a prominent class for the NO_3RR,[110,111] with Co SAs embedded in ENFs demonstrating exceptional performance. For example, Zhu, Du, and co-workers prepared a Co–C_3O_1 coordinated structure by thermally migrating Co atoms from Co NPs onto a carbon support.[70] The resulting Co SA/CNF catalyst achieves high NO_3RR properties, with a FE of 91.3% and an NH_3 production rate of 0.79 mmol h^{-1} cm^{-2} in a 0.1 M K_2SO_4 electrolyte containing 0.1 M KNO_3, greatly outperforming Co NPs/CNFs and many other reported works (Fig. 10a–d). The Co SA/CNF catalyst also possesses a superior stability, maintaining consistent activity over fifteen consecutive cycles (Fig. 10e). Theoretical calculations attribute this performance to the preferred *NO → *NOH pathway, facilitated by the optimal adsorption energy between Co-SA and *NO, enabling easy hydrogenation and deoxygenation of *NO on Co-SAs (Fig. 10f). The research reveals that the modest energy barrier from *NO to *NOH (0.45 eV) is the RDS, coupled with an effective suppression of the HER. The charge transfer properties further indicate the favorable *NO hydrogenation and deoxygenation on Co SAs (Fig. 10g). These mechanistic advantages collectively enhance NH_3 production. Additionally, a report demonstrates that atomic-level incorporation of bismuth (Bi) dramatically

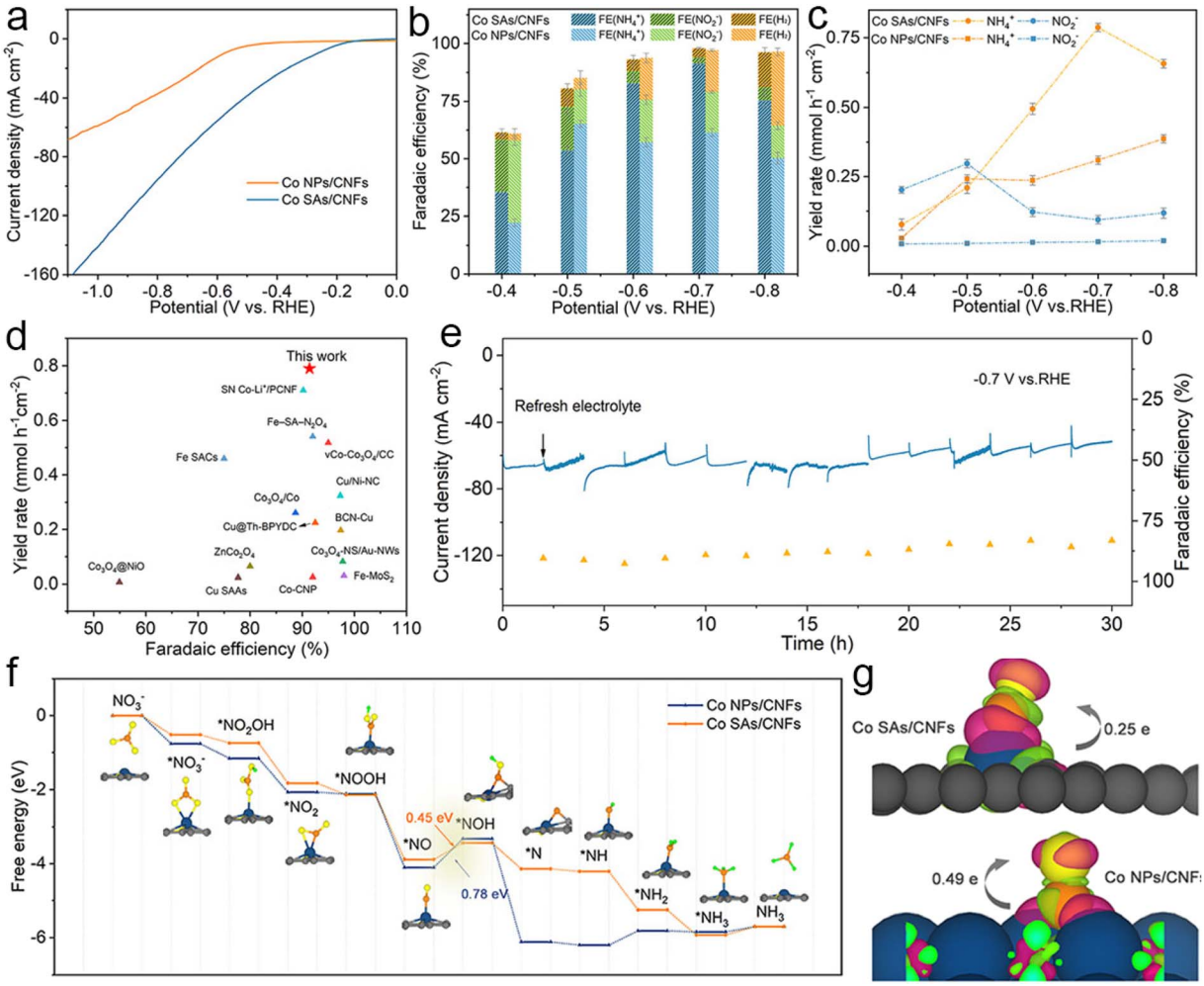

Fig. 10 (a) LSV plots of varied catalysts in K_2SO_4 (0.5 M) in the presence of KNO_3 (0.1 M). (b) FEs of NH_4^+, NO_2^- and H_2 at different potentials for varied catalysts. (c) NH_4^+ and NO_2^- yield rates at different potentials for varied catalysts. (d) Comparison of FE and yield rate of NH_4^+ on Co SAs/CNFs with previous catalysts. (e) Durability measurement and corresponding FEs of NH_4^+ from the Co SA/CNF catalyst. (f) Free energies of different pathways on varied catalysts. (g) Bader charge analysis of the *NO intermediate on varied catalysts. Reproduced with permission.[70] Copyright 2024, The Royal Society of Chemistry.

enhances the NO_3RR performance of the $CuCo_2O_4$ nanofibers, which is attributed to the reduced reaction barrier for $*NO_2$ to $*NO_2H$ conversion, improved mass transfer facilitating $*NH_3$ desorption, and reactivation of surface-active sites.[112]

5.7 Battery and electrolysis devices

5.7.1 Zn–air battery. The Zn–air battery stands out as an ideal power source, noted for its compact dimensions and high charge capacity, capable of powering flexible electronic devices, and offers the benefits of low cost, high-energy density, and safety reliability.[113] However, the current development is hindered by the sluggish kinetics of the ORR and OER at the air electrode, resulting in suboptimal energy efficiency, elevated overpotentials, and reduced charge–discharge stability. Consequently, the development of high-performance electrocatalysts is crucial for enhancing the performance of zinc–air batteries. Recently, SACs have emerged as a promising avenue in the advancement of electrode catalysts for zinc–air batteries, with SA-ENF catalysts offering distinct advantages in this regard.[33,42,62,68,73,114–126]

A catalyst with Co SAs embedded in CNFs has recently been synthesized through an innovative impregnation–carbonization–acidification strategy and deployed in Zn–air battery systems. Using ZIFs and ENFs as the precursors, this method ensures the uniform distribution of atomic Co sites within the fiber matrix following particle removal.[118] As a self-supported electrode, the Co SA-based battery exhibits an open-circuit voltage of 1.461 V, a peak power density of 61.5 mW cm^{-2}, and retains a stable discharge–charge voltage gap under different bending angles, showcasing the excellent performance and application potential in flexible Zn–air batteries.

Concurrently, a Janus-structured flexible catalyst comprising Ni SAs within hollow CNFs coupled with Co_3O_4@$Co_{1-x}S$ nanosheet arrays (Ni-SAs/HCNFs/Co-NAs) has been successfully

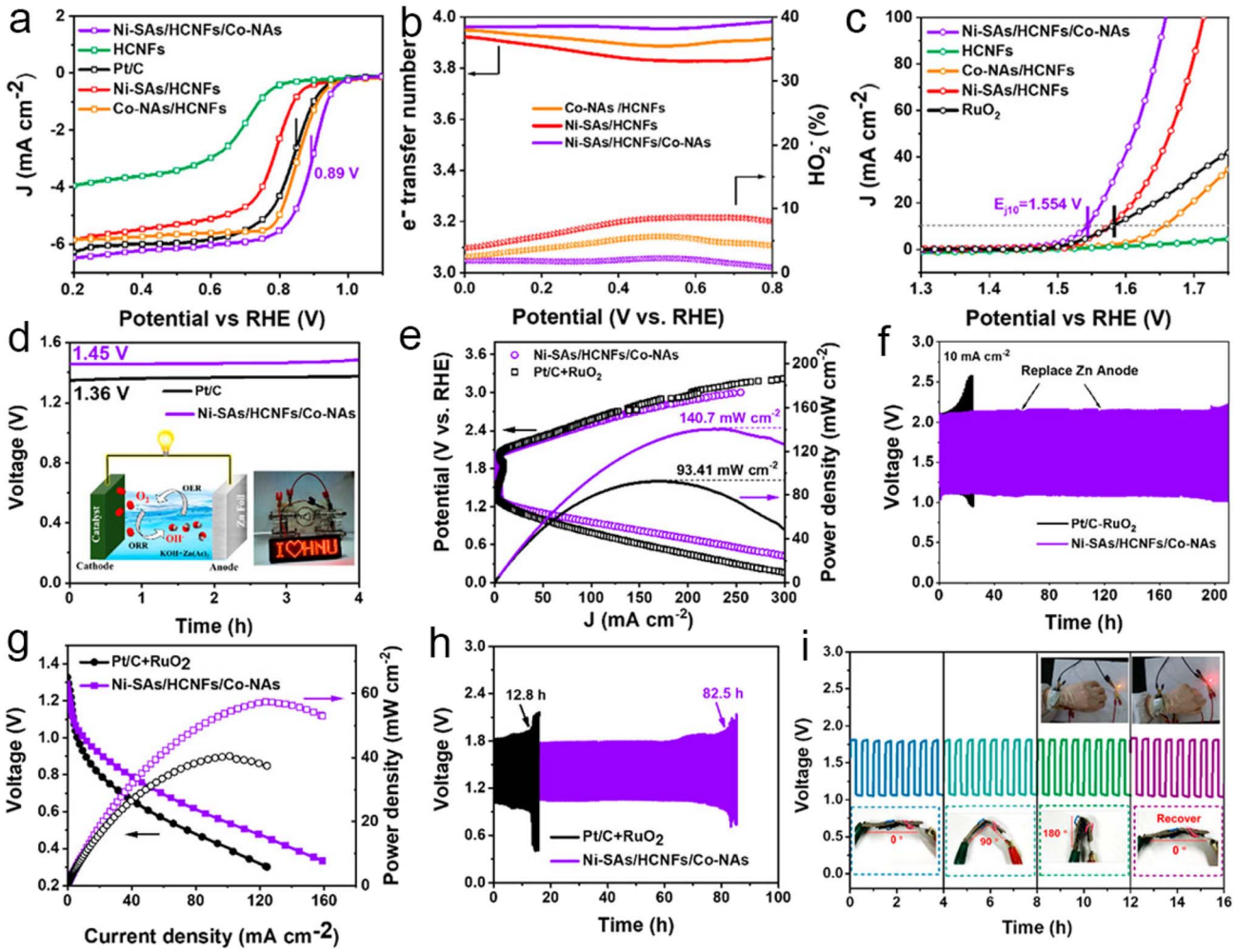

Fig. 11 (a) LSV plots and (b) electron transfer number along with HO_2^- percentage for the ORR. (c) LSV plots for the OER. (d) Open-circuit voltage curves accompanied by diagrams of the Zn–air battery and the demonstration of a power source for a display screen. (e) Charge–discharge polarization curves and corresponding power density curves. (f) Cycling stability of a Zn–air battery at 10 mA cm^{-2}. (g) Discharge polarization curves and the associated power density plots. (h) Galvanostatic cycling measurements at 10 mA cm^{-2} for varied systems. (i) Cycling stability of a solid-state flexible Zn–air battery under various bending angles and its practical application. Reproduced with permission.[127] Copyright 2022, American Chemical Society.

Table 4 Comparisons of SA-ENF catalysts for Zn–air batteries

Catalysts	Power density (mW cm^{-2})	Cycling condition (mA cm^{-2})	Cyclability evaluation	Charge/discharge voltage gaps (V) at a certain current density (mA cm^{-2})	Coordination motifs	Reference
Fe/SNCFs-NH_3	255.84	1	1000 cycles (1000 h)	0.78@5	Fe–N_4/C	33
Fe SACs@PNCNFs	163	5	200 h	0.8	Fe–N_3P_1	42
M–Fe/NPCNFs-900	169.6	10	1000 h	0.84	Fe–N_4/C	62
H–CoFe@NCNF	202	2	1100 h	0.9	$Co_{5.47}N$/Fe–N_4–N	68
g-C_3N_4–Co@CNT/Co–N_4/C	310	2	>100 h	0.75 V at 0 hours, 0.81 V at 300 hours, and 0.87 V at 800 hours	g-C_3N_4–Co@CNT/Co–N_4/C	73
Fe-SA/NCF	119.9	—	—	—	Fe–N_4	114
Co SA@NCF/CNF	—	6.25	More than 90 cycles (>15 h) at	0.6	Co–N_4	115
Co SA/NCFs	154.5	10	600 h	—	Co–N_4	116
Fe_2O_3/FeN_x@CNF	154	10	20 h with a 20 min cycling period	1.01	—	117
Co–N–CCNFMs/C	90.3	2	38 h	0.8	Co–N_4	118
Fe/NCNFs	—	5 1	10 min with 2000 cycles 1000 cycles	0.65	Fe–N_4	119
Co_{SA}Ni-NCNT/CNF	78.65	10	120 h	0.66	$N_{3/4}$–M_x	120
FeSA@HPCF	186	10	275 h	1.51	Fe–N_4	121
FeMn–N–C	151	10	700 h	1.01	Fe–N_4/Mn–N_4	122
Fe SAC/HCNF	112.9	5	600 h	0.8	Fe–N_4	123
$FeCoO_x$/Fe–N–C	184.8	50	>30 h	—	Fe–N_4	124
Zn–N_4-HPCNFs	130.2	—	—	—	Zn–N_4	125
Co,Ni-SAs/S,N-CNFs	175	1	70 h	0.9	CoN_3S_1–NiN_3S_1	126
Ni-SAs/HCNFs/Co-NAs	57.6	10	82 h	0.75	Ni–N_3O_1 and Ni–N_4	127

synthesized.[127] This architecture leverages Ni SAs to coordinate with O and N for efficient ORR ($E_{onset} = 0.99$ V, $E_{1/2} = 0.89$ V, $4e^-$ pathway) (Fig. 11a and b), while the integrated nanosheet arrays within the composite material drive the OER process ($\eta_{10} = 314$ mV) (Fig. 11c). In a liquid zinc–air battery, it delivers a superior open-circuit potential of 1.45 V, a power density of 140.7 mW cm^{-2}, a high specific capacity of 806.8 mA h g^{-1}, and an extraordinary durability of 220 hours, completely surpassing the Pt/C + RuO_2 benchmark (Fig. 11d–f). Owing to the self-supporting nature, the Ni-SA/HCNF/Co-NA catalyst is further utilized as a cathode to assemble into flexible an all-solid-state Zn–air battery, demonstrating viability in portable and wearable devices (Fig. 11g–i).

Another recent study has demonstrated the fabrication of diatomic FeMn–N–C catalysts as cathode materials for zinc–air batteries.[122] The incorporation of Mn SAs is used to strengthen Fe–N bonds and suppress the electrochemical dissolution of Fe, thereby exhibiting exceptional ORR activity. When configured into zinc–air batteries, this system achieves a peak power density of 151 mW cm^{-2} while maintaining remarkable cycling stability over 700 hours. Furthermore, the assembled zinc–air battery exhibits superior low-temperature performance, demonstrating promising potential for operation under extreme environmental conditions. Table 4 advances the recent progress in typical SA-ENF catalysts exhibiting high activity and stability in the Zn–air systems.

5.7.2 Fuel cell. Fuel cells are electrochemical devices that directly convert the chemical energy of fuels into electricity, capable of surpassing the Carnot cycle limitations of traditional heat engines, thereby achieving exceptionally high energy conversion efficiency with minimal environmental pollution. A typical fuel cell consists of an anode, a cathode, and an electrolyte membrane, where the anode facilitates fuel oxidation reactions and the cathode drives the ORR. These systems have

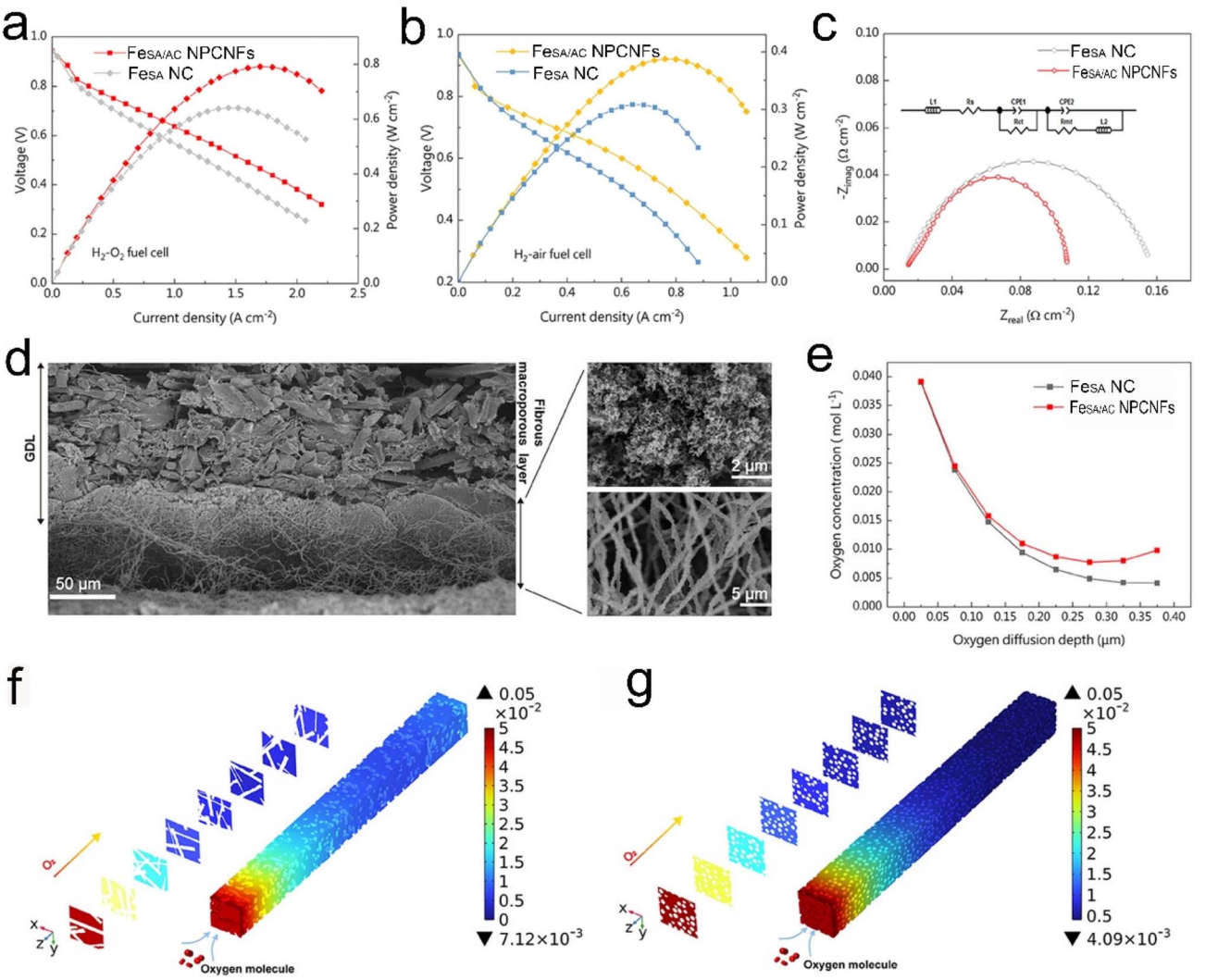

Fig. 12 Fuel cell polarization curves of Fe_{SA} NC and $Fe_{SA/AC}$ NPCNFs under (a) oxygen conditions and (b) air conditions. (c) Nyquist diagram for the fuel cell impedance measured at a constant current density of 1.5 A cm^{-2}. (d) SEM section images of the prepared $Fe_{SA/AC}$ NPCNF cathode. (e) The transient distribution curve of oxygen concentration on the cathode side with oxygen diffusion depth. Finite element simulation results of the transient distribution of oxygen concentration on the cathode side of the 3D model: (f) $Fe_{SA/AC}$ NPCNFs and (g) Fe_{SA} NC. Reproduced with permission.[129] Copyright 2025, John Wiley and Sons.

emerged as a critical technology in the field of power generation. However, the sluggish kinetics of the ORR at the cathode currently necessitate the use of high-loading Pt-based catalysts. Consequently, the development of SACs to reduce catalyst usage while enhancing fuel cell performance represents a vital research direction for their large-scale application.

In recent years, numerous studies have demonstrated that metal–N–C catalysts serve as ideal alternative materials for the cathodic ORR in PEMFCs.[128] A representative example involves the fabrication of Fe SAs and Fe clusters ($Fe_{SA/AC}$) supported on NPCNFs through electrospinning coupled with NH_3 activation pyrolysis, which exhibits an exceptionally large specific surface area (570 $m^2 g^{-1}$).[129] EXAFS analysis confirms the coexistence of Fe SAs and Fe clusters in the catalyst, demonstrating excellent $4e^-$ ORR characteristics. When assembled into membrane electrode component (MEA) as the cathode in fuel cell, the electrocatalyst achieves a remarkably larger peak power density than conventional Fe SA catalysts (Fig. 12a and b). The unique hierarchical porous nanofiber structure facilitates efficient electron transport, reflecting by the significantly reduced charge transfer impedance (Fig. 12c). Based on cross-sectional SEM images of the actual membrane electrode (Fig. 12d), a finite element numerical simulation-based 3D theoretical model of the catalyst featuring an interpenetrating long fiber laminated architecture is established. Computational results reveal that the $Fe_{SA/AC}$ NPCNF catalyst exhibits a more gradual oxygen concentration decline gradient with increasing diffusion distance compared to the Fe SA catalyst (Fig. 12e), confirming its superior mass transport properties. Furthermore, 3D simulations provide direct visualization of transient oxygen concentration profiles in both models (Fig. 12f and g), demonstrating that the engineered macroporous architecture in the $Fe_{SA/AC}$ NPCNFs dramatically mitigates oxygen diffusion limitations.

5.7.3 Overall water electrolysis. As previously discussed, ENF catalysts hold substantial promise for the HER and OER, positioning them as prime candidates for water electrolysis systems.[130–132] A recent advance involves manipulating the coordination environment to fabricate SA-ENF catalysts capable of bifunctional HER and OER activity.[133] By incorporating heteroatoms (including N, N–B, N–P, and N–S) into the porous CNFs (PCNFs), the Ni d-band center is precisely tuned,

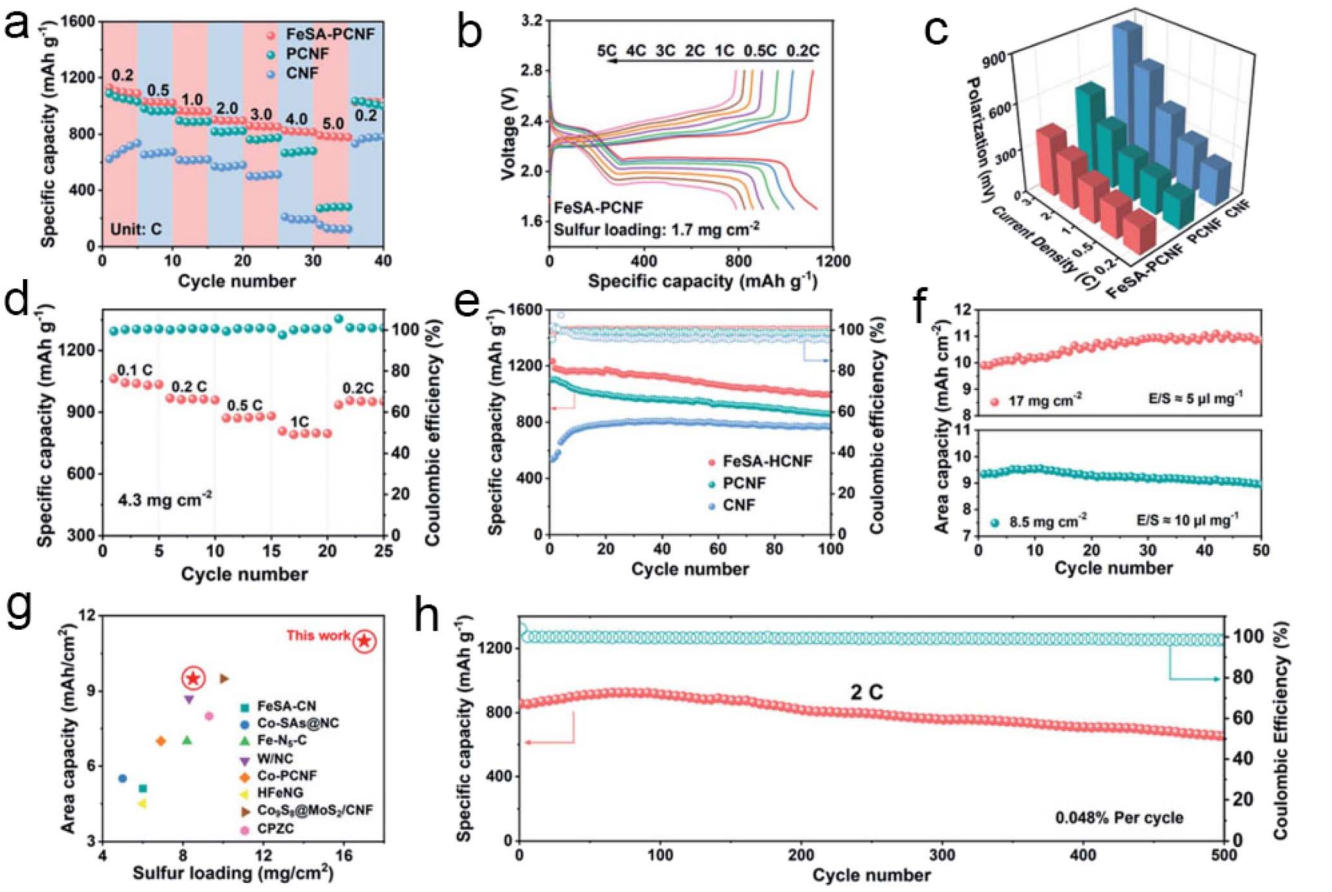

Fig. 13 (a) Rate capabilities of Li–S batteries utilizing varied cathode materials. (b) Galvanostatic charge–discharge profiles for the FeSA-PCNF cathode under various rates. (c) Voltage polarization across diverse cathodes at varied current rates. (d) Rate properties of the FeSA-PCNF cathode with a S loading of 4.3 mg cm^{-2}. (e) Cycling stability of various cathodes with a S loading of 1.7 mg cm^{-2} at 0.2C. (f) Performances with large S loadings of 8.5 and 17 mg cm^{-2} at 0.1C. (g) Comparison of the area capacity between the current study and previously reported S cathodes. (h) Long-term cycling performance of the FeSA-PCNF cathode at 2C. Reproduced with permission.[137] Copyright 2022, The Royal Society of Chemistry.

optimizing the geometric and electronic configurations of isolated Ni atoms. This adjustment effectively modulates the interactions between the Ni active sites and water splitting intermediates, enhancing the electrocatalytic efficiency. EXAFS analysis indicates that the coordination numbers for Ni–N and Ni–P are 3 and 1.1, respectively, pointing to the establishment of a Ni–N_3–P configuration. Theoretical insights suggest that the d-band center of this configuration facilitates optimal adsorption of H- and O-containing intermediates, thereby enhancing the HER and OER kinetics. This catalyst has demonstrated remarkable performance in both the HER and OER. When deployed as the cathode and anode in an overall water-splitting electrolysis cell, it requires a mere voltage of 1.67 V to reach 10 mA cm^{-2}, outperforming Ni–N/PCNFs (1.77 V), Ni–N,B/PCNFs (1.73 V), and Ni–N,S/PCNFs (1.71 V). Additionally, the cell maintains stable operation for 10 hours at 10 mA cm^{-2} with minimal voltage escalation, underscoring its robust stability. Beyond CNFs, NiMn-LDH/PAN nanofibers are also good candidates to load Ir SAs and clusters, realizing a remarkable overall water splitting efficiency in an alkaline environment.[134]

5.7.4 Li battery

5.7.4.1 Li–S battery. The Li–S battery boasts an impressive theoretical energy density of 2600 W h kg^{-1}, which highlights its potential as a promising eco-friendly energy storage system. However, the practical application of sulfur in this battery is hindered by its poor utilization and cycling instability, which induce undesirable volumetric expansion during operation. These limitations impede commercial adoption of Li–S battery technology. Notably, SACs with transition metal-derived M–N–C coordination motifs demonstrate significant potential to enhance the electrochemical behavior of sulfur.[72,135,136]

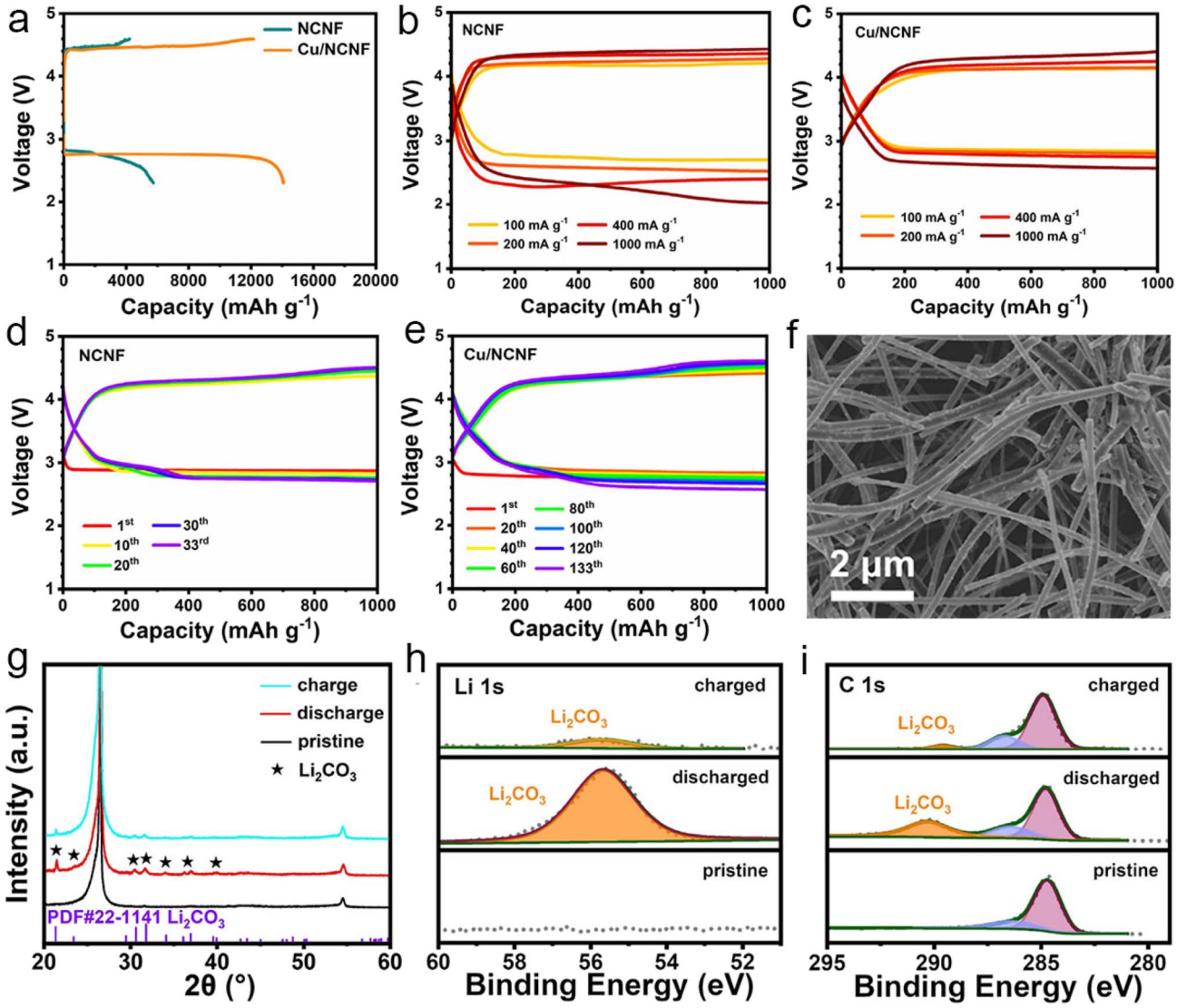

Fig. 14 (a) Comprehensive galvanostatic charge/discharge characteristics of NCNFs and Cu/NCNFs. (b and c) Galvanostatic discharge/charge profiles of NCNFs and Cu/NCNFs at varied current densities. (d and e) Cycle performances of NCNF and Cu/NCNF cathodes at 400 mA g^{-1}. (f) SEM image of the recharged Cu/NCNF material. (g) XRD pattern and XPS spectra of (h) Li 1s and (i) C 1s for the Cu/NCNF cathode under different states. Reproduced with permission.[55] Copyright 2022, Elsevier.

1D nanofibrous materials represent an emerging class of sulfur host with distinct advantages for catalyzing lithium polysulfides conversion. Thus, PCNFs functionalized with atomically dispersed Fe SAs (FeSA-PCNF), fabricated through electrospinning and pyrolysis, serve as autonomous and binder-free cathodes for Li–S batteries.[137] This advanced catalyst features an interconnected fibrous matrix with hierarchical porosity and a specific surface area of 669.5 $m^2\ g^{-1}$, ensuring rapid charge transfer kinetics and abundant active surfaces for efficient polysulfide transformation. The EXAFS spectrum verifies the atomic dispersion of Fe atoms within Fe–N(O) coordination. Equipped with this catalyst as a cathode, the constructed Li–S battery delivers exceptional rate capability (791 mA h g^{-1}) at 5C (Fig. 13a). The discharge/charge voltage profiles corroborate the formation of lithium polysulfides and sulfides (Fig. 13b). The voltage polarization observed between the charging and discharging curves for this catalyst is minimal, surpassing PCNF and CNF controls (Fig. 13c). The synergistic combination of Fe SAs and the distinct porous structure of CNFs endows the system with superior rate properties and cycling stability (Fig. 13d and e). Notably, at an elevated sulfur loading of 17 mg cm^{-2} and a reduced electrolyte-to-sulfur ratio of 5 mL mg^{-1}, the battery sustains an impressive areal capacity of 11.1 mA h cm^{-2} after 50 cycles (Fig. 13f), which is on par with previously documented high-loading S cathodes (Fig. 13g). Additionally, following 500 cycles at 2C, it displays a minimal capacity decay of merely 0.048% per cycle, demonstrating exceptional practical potential for advanced Li–S batteries (Fig. 13h). Recently, Co–N_3S_1 SAs embedded within SeS-PAN ENFs have demonstrated exceptional performance as the cathode for Li–S batteries, retaining 545.8 mA h g^{-1} at 1C with 99.24% capacity retention over 1000 cycles. This superior performance originates from the high electronegativity of S to modulate the asymmetric coordination environment of Co atoms, which enhances metal-polysulfide affinity and effectively lowers electrocatalytic energy barrier.[138]

5.7.4.2 Li–Se battery. Compared to Li–S batteries, Li–Se batteries have garnered extensive attention for their elevated specific capacity and superior electrical conductivity of the cathodic Se. However, their commercialization and performance optimization face several key challenges, notably the intrinsic low reactivity of selenium, significant volume changes during cycling, and the deleterious shuttle effect induced by polyselenides. Recent work demonstrates that Mo SAs embedded in CNFs *via* high-temperature inert-atmosphere pyrolysis serve as high-performance Li–Se battery electrodes.[139] The resulting catalyst features pronounced internal channels from thermal decomposition of PMMA in the precursors. HAADF-STEM confirms uniform atomic Mo distribution throughout the matrix, while EDS measurement quantifies the Mo loading at 5.94%. After Se incorporation, the electrode sustains a specific capacity of 535 mA h g^{-1} over 500 cycles at 1C, achieving 82% capacity retention with minimal capacity decay (0.36% per cycle). Remarkably, at the demanding discharge rate of 5C, the catalyst demonstrates a minimal loss in capacity, underscoring its exceptional high-rate resilience. This study establishes novel pathways for advancing high-capacity energy storage systems.

5.7.4.3 Li–CO_2 battery. Li–CO_2 batteries have recently captured considerable interest due to their high theoretical energy density and potential for CO_2 utilization. However, the high charging voltage impedes operation at practical current densities, resulting in diminished energy efficiency.[55] As established, SA-ENF catalysts have shown remarkable CO_2RR performance, with Cu SA catalysts demonstrating significant promise. Accordingly, Cu SAs embedded in NCNF catalysts are successfully synthesized *via* electrospinning and ammonia-assisted pyrolysis. The resulting Cu SA-based catalyst acts as a self-supporting electrode for Li–CO_2 batteries. AC HAADF-STEM confirms the exclusive presence of isolated Cu sites, while ICP analysis quantifies a Cu loading of 1.54 wt% within the catalyst. EXAFS spectroscopy further elucidates a well-defined Cu–N_4 coordination environment. This structure effectively facilitates the adsorption and activation of CO_2 molecules. In Li–CO_2 battery testing, this Cu SA-based electrode showcases an impressive capacity of 14 084 mA h g^{-1} at a current density of 100 mA g^{-1} and a minimal overpotential of 1.29 V (Fig. 14a–c), significantly surpassing the performance of NCNFs. Moreover, the battery demonstrates robust cycling stability, achieving up to 133 cycles, which is a substantial improvement over the cell equipped with NCNFs alone (Fig. 14d and e). Subsequent characterization studies reveal that the discharge product, Li_2CO_3, is efficiently decomposed during the charging process (Fig. 14f–i). This work establishes a dual-functional catalyst system that simultaneously enables efficient CO_2 utilization and high-performance energy storage.

6. Conclusions and outlook

This review first examines the structural advantages of SA nanofibrous materials, then explores their precision synthesis and cutting-edge developments in electrocatalysis. SA-ENFs synergistically combine the merits of SAs and nanofibrous architectures while facilitating hierarchical porosity that markedly improves the electrocatalytic reaction kinetics. The incorporation of SAs delivers substantial electrocatalytic enhancement, positioning these catalysts for growing scientific and technological recognition in the coming years. Despite demonstrated applications and achievements in SA-ENF systems, their long-term advancement faces both significant challenges and untapped opportunities.

(1) A fundamental challenge lies in reconciling high atomic dispersion with elevated metal loading capacity. Metal atoms exhibit extremely high surface free energy, driving their tendency to undergo aggregation into nanoparticles or clusters during synthesis and catalytic operation. In SA-ENF catalysts, atomic dispersion primarily depends on defect sites or dopants, such as N-coordination motifs in CNFs, yet these anchoring sites possess inherently limited density. As metal loading increases, the support cannot provide sufficient spatial confinement to prevent atomic agglomeration. Achieving high-loading SACs necessitates optimization of metal–support interactions and coordination environments. Implementing

multilevel stabilization and sub-atmospheric pressure annealing strategies may prove effective in attaining this objective.

(2) Significant bottlenecks persist in characterization methodologies. Although techniques such as AC HAADF-STEM and XAFS effectively resolve SA configurations, they face challenges in monitoring the real-time dynamic evolution of active sites during catalytic reactions. This critical gap substantially impedes mechanistic understanding of complex electrocatalytic processes, particularly under an intrinsic reconstruction process. Developing advanced *in situ* characterization technologies is therefore imperative to directly probe actual active-site structural details and capture reaction dynamics. Such innovations would establish fundamental process–structure–performance relationships, bridging knowledge deficits under practical operating conditions.

(3) Improving the mechanical robustness of non-carbon nanofiber catalysts is a critical priority. These materials exhibit inherent microscale brittleness, fracturing readily under mechanical stress and compromising electrode stability. Free-standing electrodes require strong interfacial interactions among the crystallinity domains of non-carbon materials such as metal oxides and sulfides to maintain structural integrity. However, weak interfacial bonding of these materials causes inevitable delamination during bending or tensile strain. Future advancements must integrate innovative material architectures with advanced manufacturing technologies to overcome these micromechanical limitations.

(4) Significant stability challenges persist in practical implementations. Despite advancing deployment of SA-ENF catalysts in energy catalysis systems, critical issues remain unresolved, including SA agglomeration tendencies, metal migration from weak metal–support interactions, and atomic leaching with coordination environment degradation under harsh electrochemical conditions such as acidic, alkaline, and strongly oxidizing media. Developing durable catalysts necessitates multipronged strategies, such as strengthening metal–support bonding, optimizing support matrix stability, and engineering in situ-formed self-healing bonds during operation to achieve long-term atomic stabilization.

Author contributions

Bingyan Shi collected references and prepared the initial draft; Xiaofeng Lu conceived the idea for this review and revised the manuscript.

Conflicts of interest

The authors declare no conflict of interest.

Data availability

No primary research results, software or code have been included and no new data were generated or analyzed as part of this review.

Acknowledgements

This work was financially supported by the National Natural Science Foundation of China (No. 52473034) and the Jilin Province Science and Technology Development Program (YDZJ202501ZYTS305).

References

1 T. Maschmeyer, F. Rey, G. Sankar and J. M. Thomas, *Nature*, 1995, **378**, 159–162.
2 K. Asakura, H. Nagahiro, N. Ichikuni and Y. Iwasawa, *Appl. Catal., A*, 1999, **188**, 313–324.
3 B. Qiao, A. Wang, X. Yang, L. F. Allard, Z. Jiang, Y. Cui, J. Liu, J. Li and T. Zhang, *Nat. Chem.*, 2011, **3**, 634–641.
4 K. Jiang, Z. Liu, Y.-R. Lu, M. Wang, D. Chen, L. Cai, T.-S. Chan, P. Liu, A. Pan and Y. Tan, *Adv. Mater.*, 2023, **35**, 2207850.
5 V. Muravev, A. Parastaev, Y. van den Bosch, B. Ligt, N. Claes, S. Bals, N. Kosinov and E. J. M. Hensen, *Science*, 2023, **380**, 1174–1179.
6 F. Zhang, Y. Zhu, Q. Lin, L. Zhang, X. Zhang and H. Wang, *Energy Environ. Sci.*, 2021, **14**, 2954–3009.
7 Y. Shang, X. Xu, B. Gao, S. Wang and X. Duan, *Chem. Soc. Rev.*, 2021, **50**, 5281–5322.
8 C. Peng, R. Pang, J. Li and E. Wang, *Adv. Mater.*, 2024, **36**, 2211724.
9 P. Liu, Y. Zhao, R. Qin, S. Mo, G. Chen, L. Gu, D. M. Chevrier, P. Zhang, Q. Guo, D. Zang, B. Wu, G. Fu and N. Zheng, *Science*, 2016, **352**, 797–800.
10 F. Chen, L.-L. Liu, J.-H. Wu, X.-H. Rui, J.-J. Chen and Y. Yu, *Adv. Mater.*, 2022, **34**, 2202891.
11 X. Li, J. Ding, Z. Yu, L. Xu, J. Zhao, J. Chen and S. Dong, *CCS Chem.*, 2025, **7**, 776–785.
12 N. Lazaar, S. Wu, S. Qin, A. Hamrouni, B. Bikash Sarma, D. E. Doronkin, N. Denisov, H. Lachheb and P. Schmuki, *Angew. Chem., Int. Ed.*, 2025, **64**, e202416453.
13 M. Zhang, W. Zhu, Z. Liu, S. Chen, D. Zhou, X. Mu, Z. Zhuang, S. Wang, J. Yang, Y. Du, X. Luo, Q. Zhang, S. Liu, D. Wang and Z. Dai, *Angew. Chem., Int. Ed.*, 2025, **64**, e202510206.
14 N. Song, S. Ren, Y. Zhang, C. Wang and X. Lu, *Adv. Funct. Mater.*, 2022, **32**, 2204751.
15 D. Ji, Y. Lin, X. Guo, B. Ramasubramanian, R. Wang, N. Radacsi, R. Jose, X. Qin and S. Ramakrishna, *Nat. Rev. Methods Primers*, 2024, **4**, 1.
16 G. I. Taylor, *Proc. R. Soc. London, Ser. A*, 1964, **280**, 383–397.
17 X. Gong, J. Yu, X. Liu, J. Yu, S. Zhang and B. Ding, *Adv. Funct. Mater.*, 2024, **34**, 2316030.
18 Y. Wang, Q. Jiang, S. Ren, J. Xu, Y. Wang, M. Zhong and X. Lu, *Adv. Mater.*, 2025, **37**, 2504922.
19 C. Wang, W. Wang, H. Qi, Y. Dai, S. Jiang, B. Ding, X. Wang, C. Li, J. Zeng, T. Wu, H. Li, Y. Wang, Y. Zhao, W. Wang, Z. Li, X. Mo, H. Hou, L. Dong, H. Ma, Y. Liu, C. Su, J. Bai, W. Wu, G. Guo, G. Nie, N. Wang, H. Zhu, J. Bai, J. Fang, D. Liang, Z. Bai, G. Han, X. Lu, K. Wang, X. Zhang, W. Kang, N. Deng, W. Hu, W. Chen, X. Zhang, D. Yang,

F. Wang, Y. Bian, Z. Liu, L. Zhang, X. Li, L. Li, Y. Li, H. Huang, X. Jia, X. Li, D. Yang, X. Jin, S. Li, X. Zhang, N. Tang, R. Hao, F. Tian, L. Mai, Y. Wei and J. Xue, *Prog. Mater. Sci.*, 2025, **154**, 101494.
20 X. Li, X. Zhang, F. Su, H. Zhao, Z. Qu, C. Ge and J. Fang, *Nanoscale*, 2025, **17**, 8999–9020.
21 W. Song, M. Li, C. Wang and X. Lu, *Carbon Energy*, 2021, **3**, 101–128.
22 Y. Cho, J. W. Beak, M. Sagong, S. Ahn, J. S. Nam and I. D. Kim, *Adv. Mater.*, 2025, **37**, 2500162.
23 D. Kong, W. Guo, Y. Zhao and Y. Zhao, *Adv. Energy Mater.*, 2025, **15**, 2403983.
24 Y. Lei, Q. Wang, S. Peng, S. Ramakrishna, D. Zhang and K. Zhou, *Adv. Energy Mater.*, 2020, **10**, 1902115.
25 B. Muthukutty, P. Sathish Kumar, D. Lee and S. Lee, *ACS Nano*, 2024, **18**, 27287–27316.
26 P. R. Ilango, A. D. Savariraj, H. Huang, L. Li, G. Hu, H. Wang, X. Hou, B. C. Kim, S. Ramakrishna and S. Peng, *Electrochem. Energy Rev.*, 2023, **6**, 12.
27 W. Li, R. Liu, G. Yu, X. Chen, S. Yan, S. Ren, J. Chen, W. Chen, C. Wang and X. Lu, *Small*, 2024, **20**, e2307164.
28 M. Zhong, J. Yang, M. Xu, S. Ren, X. Chen, C. Wang, M. Gao and X. Lu, *Small*, 2024, **20**, 2304782.
29 L. Ye, S. Qi, T. Cheng, Y. Jiang, Z. Feng, M. Wang, Y. Liu, L. Dai, L. Wang and Z. He, *ACS Nano*, 2024, **18**, 18852–18869.
30 Y. Han, H. Duan, W. Liu, C. Zhou, B. Wang, Q. Jiang, S. Feng, W. Yan, T. Tan and R. Zhang, *Appl. Catal., B*, 2023, **335**, 122898.
31 X. Ren, H. Liu, J. Wang and J. Yu, *Chin. Chem. Lett.*, 2024, **35**, 109282.
32 H. Zhao, C. Zhang, H. Li and J. Fang, *Nano Sel.*, 2021, **2**, 2072.
33 L. Yang, X. Zhang, L. Yu, J. Hou, Z. Zhou and R. Lv, *Adv. Mater.*, 2022, **34**, 2105410.
34 J. Yu, J. Li, C.-Y. Xu, Q. Liu, J. Liu, R. Chen, J. Zhu, R. Li and J. Wang, *Carbon*, 2021, **185**, 96–104.
35 T. Li, T. Lu, X. Li, L. Xu, Y. Zhang, Z. Tian, J. Yang, H. Pang, Y. Tang and J. Xue, *ACS Nano*, 2021, **15**, 20032–20041.
36 C.-K. Hwang, S. Kim, K. R. Yoon, T. T. Le, C. V. Hoang, J. W. Choi, W. Zhang, S. Y. Paek, C. H. Lee, J. H. Lee, K. H. Chae, S. Jeong, S. Y. Lee, B.-K. Ju, S. H. Kim, S. S. Han and J. M. Kim, *Carbon Energy*, 2024, **6**, e582.
37 L. Dong, J. Zang, W. Wang, X. Liu, Y. Zhang, J. Su, Y. Wang, X. Han and J. Li, *J. Colloid Interface Sci.*, 2020, **564**, 134–142.
38 H. Chuai, H. Yang and S. Zhang, *ACS Appl. Mater. Interfaces*, 2024, **16**, 24823–24830.
39 L. Chen, X. Wang, T. Lu, H. Pang, S. Zhang, L. Xu, G. Yang, Q. Zhou and Y. Tang, *Appl. Catal., B*, 2025, **366**, 125007.
40 Q. Luo, K. Wang, Q. Zhang, W. Ding, R. Wang, L. Li, S. Peng, D. Ji and X. Qin, *Angew. Chem., Int. Ed.*, 2025, **64**, e202413369.
41 C. Cai, K. Liu, L. Zhang, F. Li, Y. Tan, P. Li, Y. Wang, M. Wang, Z. Feng, D. Motta Meira, W. Qu, A. Stefancu, W. Li, H. Li, J. Fu, H. Wang, D. Zhang, E. Cortés and M. Liu, *Angew. Chem., Int. Ed.*, 2023, **62**, e202300873.
42 Y. Liu, H. Liu, L. Li, Y. Tang, Y. Sun and J. Zhou, *Small*, 2025, **21**, 2501495.
43 Y.-X. Xiao, J. Ying, J.-B. Chen, Y. Dong, X. Yang, G. Tian, J. Wu, C. Janiak, K. Ozoemena and X. Yang, *Chem. Mater.*, 2022, **34**, 3705–3714.
44 H. Wang, H. Chuai, X. Chen, J. Lin, S. Zhang and X. Ma, *ACS Appl. Mater. Interfaces*, 2023, **15**, 1376–1383.
45 H. Yang, Y. Wu, G. Li, Q. Lin, Q. Hu, Q. Zhang, J. Liu and C. He, *J. Am. Chem. Soc.*, 2019, **141**, 12717–12723.
46 W. Zheng, Y. Wang, L. Shuai, X. Wang, F. He, C. Lei, Z. Li, B. Yang, L. Lei, C. Yuan, M. Qiu, Y. Hou and X. Feng, *Adv. Funct. Mater.*, 2021, **31**, 2008146.
47 L. Deng, L. Qiu, R. Hu, L. Yao, Z. Zheng, X. Ren, Y. Li and C. He, *Appl. Catal., B*, 2022, **305**, 121058.
48 L. Zhang, Z. Ma, Z. Wu, Y. Liu, J. Bai, S. Zhang, E. Debroye, W. Fan, H. Lin and T. Liu, *Adv. Funct. Mater.*, 2024, **34**, 2404707.
49 Z. Wu, J. Bai, F. Lai, H. Zheng, Y. Zhang, N. Zhang, C. Wang, Z. Wang, L. Zhang and T. Liu, *Sci. China Mater.*, 2023, **66**, 2680–2688.
50 T. Li, T. Lu, H. Zhong, S. Xi, M. Zhang, H. Pang, J. Yang, L. Xu, Y. Tang and J. Xue, *Adv. Energy Mater.*, 2023, **13**, 2203274.
51 L. Jiao, J. Zhu, Y. Zhang, W. Yang, S. Zhou, A. Li, C. Xie, X. Zheng, W. Zhou, S.-H. Yu and H.-L. Jiang, *J. Am. Chem. Soc.*, 2021, **143**, 19417–19424.
52 L. Yang, L. Yu, Z. Huang, F. Kang and R. Lv, *J. Energy Chem.*, 2022, **75**, 430–440.
53 R. Pang, H. Xia, X. Dong, Q. Zeng, J. Li and E. Wang, *Adv. Sci.*, 2024, **11**, 2407294.
54 W. Yang, W. Zhang, R. Liu, F. Lv, Y. Chao, Z. Wang and S. Guo, *Chin. J. Catal.*, 2022, **43**, 110–115.
55 Y. Xu, H. Gong, L. Song, Y. Kong, C. Jiag, H. Xue, P. Li, X. Huang, J. He and T. Wang, *Mater. Today Energy*, 2022, **25**, 100967.
56 Z. Zhang, J. Cai, H. Zhu, Z. Zhuang, F. Xu, J. Hao, S. Lu, H. Li, F. Duan and M. Du, *Chem. Eng. J.*, 2020, **392**, 123655.
57 X. Wang, Y. Wang, L. Cui, W. Gao, X. Li, H. Liu, W. Zhou and J. Wang, *Chin. Chem. Lett.*, 2024, **35**, 110031.
58 H. Shin, W.-G. Jung, D.-H. Kim, J.-S. Jang, Y. H. Kim, W.-T. Koo, J. Bae, C. Park, S.-H. Cho, B. J. Kim and I.-D. Kim, *ACS Nano*, 2020, **14**, 11394–11405.
59 J. Jones, H. Xiong, A. T. DeLaRiva, E. J. Peterson, H. Pham, S. R. Challa, G. Qi, S. Oh, M. H. Wiebenga, X. I. Pereira Hernández, Y. Wang and A. K. Datye, *Science*, 2016, **353**, 150–154.
60 J. Hao, H. Zhu, Z. Zhuang, Q. Zhao, R. Yu, J. Hao, Q. Kang, S. Lu, X. Wang, J. Wu, D. Wang and M. Du, *ACS Nano*, 2023, **17**, 6955–6965.
61 Y. Gao, S. Liang, C. Jiang, M. Gu, Q. Zhang, A. Abdelhafiz, Z. Zhang, Y. Han, Y. Yang, X. Zhang, P. Liang, J. Li and X. Huang, *Sci. Adv.*, 2025, **11**, eads7154.
62 H. Zhao, B. Song, H. Li, X. Li, C. Ge, Q. Wu, J. Chen, Z. Wang, G. Yan and J. Fang, *Small*, 2025, **21**, 2407700.
63 K. Cheng, D. Shen, Y. Xia, K. Dai, C. Shao, Y. Jiang and Y. Chen, *Angew. Chem., Int. Ed.*, 2025, **64**, e202508932.

64 Z. Hao, J. Chen, X. Lu, L. Kang, C. Tan, R. Xu, L. Yuan, D. J. L. Brett, P. R. Shearing, F. R. Wang and Y. Huang, *Energy Storage Mater.*, 2022, **49**, 85–92.
65 J. Hao, Z. Zhuang, J. Hao, C. Wang, S. Lu, F. Duan, F. Xu, M. Du and H. Zhu, *Adv. Energy Mater.*, 2022, **12**, 2200579.
66 J. K. Nørskov, T. Bligaard, B. Hvolbæk, F. Abild-Pedersen, I. Chorkendorff and C. H. Christensen, *Chem. Soc. Rev.*, 2008, **37**, 2163–2171.
67 Y. Chen, S. Ji, S. Zhao, W. Chen, J. Dong, W.-C. Cheong, R. Shen, X. Wen, L. Zheng, A. I. Rykov, S. Cai, H. Tang, Z. Zhuang, C. Chen, Q. Peng, D. Wang and Y. Li, *Nat. Commun.*, 2018, **9**, 5422.
68 X. Zhang, P. Yu, G. Xing, Y. Xie, X. Zhang, G. Zhang, F. Sun and L. Wang, *Small*, 2022, **18**, 2205228.
69 S. Xia, F. Chen, Z. Shi, L. Deng, A. Georgi and H. Zhang, *Chem. Eng. J.*, 2024, **499**, 156594.
70 X. Zheng, J. Hao, Z. Zhuang, Q. Kang, X. Wang, S. Lu, F. Duan, M. Du and H. Zhu, *Nanoscale*, 2024, **16**, 4047–4055.
71 S. Nagappan, H. Minhas, R. R. Urkude, B. Pathak and S. Kundu, *Small*, 2025, **21**, 2500081.
72 Z.-F. Wang, H.-Y. Wang, X.-L. Liu, Y.-X. Chen, Y. Zhao, Y.-G. Zhang, Q.-Q. Han, C.-L. Qin, Z. Bakenov, Y.-C. Wang and X. Wang, *Rare Met.*, 2023, **42**, 3705–3717.
73 T. Lu, N. Xu, B. Zhou, L. Guo, X. Wen, S. Lou, G. Liu, W. Yang, N. Yang, M. Safari, H. Huang and J. Qiao, *eScience*, 2025, 100450.
74 X. Yu, M. Xia, R. Qi, Y. Wang, M. Gao, M. Zhong and X. Lu, *Chem. Sci.*, 2025, **16**, 10042–10050.
75 W. Li, C. Wang and X. Lu, *J. Mater. Chem. A*, 2021, **9**, 3786–3827.
76 M. Li, H. Wang, W. Zhu, W. Li, C. Wang and X. Lu, *Adv. Sci.*, 2020, **7**, 1901833.
77 A. S. Aricò, P. Bruce, B. Scrosati, J.-M. Tarascon and W. van Schalkwijk, *Nat. Mater.*, 2005, **4**, 366–377.
78 J. Chen, G. Fu, Y. Tian, X. Li, M. Luo, X. Wei, T. Zhang, T. Gao, C. Chen, S. Chaemchuen, X. Xu, X. Sun, T. Bu, F. Verpoort, J. Wang and Z. Kou, *Interdiscip. Mater.*, 2024, **3**, 595–606.
79 B. Jiang, J. Zhu, Z. Xia, J. Lyu, X. Li, L. Zheng, C. Chen, S. Chaemchuen, T. Bu, F. Verpoort, S. Mu, J. Wu, J. Wang and Z. Kou, *Adv. Mater.*, 2024, **36**, 2310699.
80 H. Ma, W. Peng, H. Wong, X. Guo, L. Xu, M. Tamtaji and Y. Ding, *Adv. Funct. Mater.*, 2024, **34**, 2409575.
81 Z. Pu, I. S. Amiinu, R. Cheng, P. Wang, C. Zhang, S. Mu, W. Zhao, F. Su, G. Zhang, S. Liao and S. Sun, *Nano-Micro Lett.*, 2020, **12**, 21.
82 H. Zhang, L. Yu, T. Chen, W. Zhou and X. W. Lou, *Adv. Funct. Mater.*, 2018, **28**, 1807086.
83 M. Li, J. Yu, Q. Liu, J. Liu, R. Chen, J. Zhu, R. Li and J. Wang, *ACS Sustain. Chem. Eng.*, 2022, **10**, 13505–13513.
84 N. Logeshwaran, G. Kim, P. Thangavel, S. S. Jeon, K. Thiyagarajan, K. R. Kishore, H. Lee, I. Seo, H. Yun, S. Lee, B.-H. Kim and Y. J. Lee, *Adv. Sci.*, 2025, **12**, 2413176.
85 W. Li, C. Wang and X. Lu, *Nano Lett.*, 2024, **24**, 11779–11792.
86 M. Xu, W. Li, M. Zhong, J. Yang, M. Gao, N. Pinna and X. Lu, *ACS Mater. Lett.*, 2024, **6**, 3548–3556.
87 T. E. Jones, D. Teschner and S. Piccinin, *Chem. Rev.*, 2024, **124**, 9136–9223.
88 Y. Yao, J. Lyu, X. Li, C. Chen, F. Verpoort, J. Wang, Z. Pan and Z. Kou, *DeCarbon*, 2024, **5**, 100062.
89 Y. Liu, W. Peng, H. Ma, J. Tian, K. Wang, Z. Zheng, L. Xu and Y. Ding, *ACS Appl. Mater. Interfaces*, 2025, **17**, 19806–19817.
90 R. Appiah-Ntiamoah and H. Kim, *ChemCatChem*, 2024, **16**, e202400786.
91 B. Cai, X. Chen, L. Wang and H. Fu, *ACS Catal.*, 2024, **14**, 13602–13629.
92 J. Tao, X. Wang, M. Xu, C. Liu, J. Ge and W. Xing, *Ind. Chem. Mater.*, 2023, **1**, 388–409.
93 Y. Yuan, Y. Zheng, D. Luo, W. Qiu, J. Wang, X. Wang and Z. Chen, *Carbon Energy*, 2024, **6**, e426.
94 E. Luo, Y. Chu, J. Liu, Z. Shi, S. Zhu, L. Gong, J. Ge, C. H. Choi, C. Liu and W. Xing, *Energy Environ. Sci.*, 2021, **14**, 2158–2185.
95 B. Ge, L. Hu, X. Yu, L. Wang, C. Fernandez, N. Yang, Q. Liang and Q.-H. Yang, *Adv. Mater.*, 2024, **36**, 2400937.
96 W. Sang, K. Liu, T. Wang, J. Lyu, Z. Nie, L. Zhang, M. Xiong, X. Li, L. Zheng, C. Chen, F. Verpoort, J. Wu, S. Mu and Z. Kou, *Nano Energy*, 2025, **138**, 110861.
97 G. Zhu, Z. Li, H. Guo, G. Li, Y. Zheng, X. Liu, H. Pan, L. Dong, J. Zang and S. Jia, *J. Alloys Compd.*, 2024, **979**, 173604.
98 F. Yan, L. Dong, J. Su, X. Liu, X. Han, J. Zang and Y. Wang, *Electrochem. Commun.*, 2022, **136**, 107245.
99 P. Liu, Y. Li, C. Sun, G. Liu, X. Wang and H. Zhao, *ACS Appl. Nano Mater.*, 2025, **8**, 7267–7277.
100 X. Zhang, P. Yu, D. Shen, B. Cai, T. Han, Y. Xie and L. Wang, *Adv. Powder Mater.*, 2025, **4**, 100288.
101 A. R. Woldu, Z. Huang, P. Zhao, L. Hu and D. Astruc, *Coord. Chem. Rev.*, 2022, **454**, 214340.
102 M. Sun, H. H. Wong, T. Wu, Q. Lu, L. Lu, C. H. Chan, B. Chen, A. W. Dougherty and B. Huang, *Adv. Energy Mater.*, 2023, **13**, 2203858.
103 R. Shi and T. Zhang, *Sci. Bull.*, 2020, **65**, 696–697.
104 H. Yang, Q. Lin, C. Zhang, X. Yu, Z. Cheng, G. Li, Q. Hu, X. Ren, Q. Zhang, J. Liu and C. He, *Nat. Commun.*, 2020, **11**, 593.
105 H. Li, L. Fang, T. Wang, R. Bai, J. Zhang, T. Li, Z. Duan, K.-J. Chen and F. Pan, *Adv. Mater.*, 2025, **37**, 2416337.
106 Z. Li, Z. Zhu, J. Wang, Y. Lin, W. Li, Y. Chen, X. Niu, X. Qi, J. Wang, J. S. Chen and R. Wu, *Adv. Funct. Mater.*, 2024, **34**, 2410552.
107 H. Wang, Y. Jin, Y. Jin, S. Kuang, T. Yan, X. Wang, X. Wang, W. Cui and S. Zhang, *AIChE J.*, 2025, **71**, e18746.
108 R. Qi, L. Zhang, S. Ren, B. Shi, M. Zhong, Z.-J. Chen and X. Lu, *Nano Lett.*, 2024, **24**, 8964–8972.
109 X. Long, T. Zhong, F. Huang, P. Li, H. Zhao, J. Fang, D. Shu and C. He, *Appl. Catal., B*, 2025, **365**, 124944.
110 R. Qi, Q. Jiang, L. Deng, X. Yu, B. Shi, M. Zhong, Y. Wang and X. Lu, *Chem. Sci.*, 2025, **16**, 378–385.
111 R. Qi, Z. Wang, M. Zhong, C. Wang, F. Bai and X. Lu, *Small*, 2024, **20**, 2308311.

112 H. Lin, J. Wei, Y. Guo, Y. Li, X. Lu, C. Zhou, S. Liu and Y. Li, *Adv. Funct. Mater.*, 2024, **34**, 2409696.
113 X. Xie, Z. Zhai, L. Peng, J. Zhang, L. Shang and T. Zhang, *Sci. Bull.*, 2023, **68**, 2862–2875.
114 W. Wang, K. Rui, K. Wu, Y. Wang, L. Ke, X. Wang, F. Xu, Y. Lu and J. Zhu, *Chem.–Eur. J.*, 2022, **28**, e202200789.
115 D. Ji, L. Fan, L. Li, S. Peng, D. Yu, J. Song, S. Ramakrishna and S. Guo, *Adv. Mater.*, 2019, **31**, 1808267.
116 Y. Han, H. Duan, C. Zhou, H. Meng, Q. Jiang, B. Wang, W. Yan and R. Zhang, *Nano Lett.*, 2022, **22**, 2497–2505.
117 M. Wang, T. Liao, X. Zhang, J. Cao, S. Xu, H. Tang and Y. Wang, *Adv. Mater. Interfaces*, 2022, **9**, 2101904.
118 Z. Xu, J. Zhu, J. Shao, Y. Xia, J. Tseng, C. Jiao, G. Ren, P. Liu, G. Li, R. Chen, S. Chen, F. Huang and H.-L. Wang, *Energy Storage Mater.*, 2022, **47**, 365–375.
119 H. Liu, C. Wang, X. Ai, B. Wang, Y. Bian, G. Wang, Y. Wang, Z. Hu and Z. Zhang, *J. Colloid Interface Sci.*, 2023, **651**, 525–533.
120 M. B. Poudel, M. P. Balanay, P. C. Lohani, K. Sekar and D. J. Yoo, *Adv. Energy Mater.*, 2024, **14**, 2400347.
121 M. Shen, L. Xie, Y. Zhang, J. Sun, Y. Jia, Y. Liu and Y. Ni, *J. Colloid Interface Sci.*, 2025, **699**, 138230.
122 C. Hu, G. Xing, W. Han, Y. Hao, C. Zhang, Y. Zhang, C.-H. Kuo, H.-Y. Chen, F. Hu, L. Li and S. Peng, *Adv. Mater.*, 2024, **36**, 2405763.
123 J. Ma, J. Li, Y. Tian, J. Liu and R. Wang, *Rare Met.*, 2025, **44**, 5412–5427.
124 K. Wei, F. Yang, Y. Sun, C. Yu, J. An, G. Ma and Y. Li, *Adv. Funct. Mater.*, 2025, **35**, 2422039.
125 Q. Wu, X. H. Chen, D. Ma, X. Xie, Y. Li, S. Xue, H. Ding, B. Liu, T. Xu and Y. Wu, *J. Mater. Chem. A*, 2025, **13**, 27326–27335.
126 H. Pan, C. Zhang, J. Wu, H. Li, T. Zhang, X. Huang, W. Tu, J. Yu, J. Dou and X. Chen, *Chem. Eng. J.*, 2024, **499**, 156345.
127 Y. Chen, S. Qiao, Y. Tang, Y. Du, D. Zhang, W. Wang, H. Zhang, X. Sun and C. Liu, *ACS Nano*, 2022, **16**, 15273–15285.
128 K. Kumar, L. Dubau, F. Jaouen and F. Maillard, *Chem. Rev.*, 2023, **123**, 9265–9326.
129 Y. Leng, Q. Han, J. Zhang, X. Lin and Z. Xiang, *Small*, 2025, **21**, 2504253.
130 L. Zhang, W. Li, S. Ren, W. Song, C. Wang and X. Lu, *Adv. Energy Mater.*, 2024, **14**, 2403136.
131 W. Li, W. Gou, L. Zhang, M. Zhong, S. Ren, G. Yu, C. Wang, W. Chen and X. Lu, *Chem. Sci.*, 2024, **15**, 11890–11901.
132 W. Li, L. Zhang, L. Ma, J. Wang, R. Qi, Y. Pang, M. Xu, C. Zhao, C. Wang, M. Gao and X. Lu, *Nano Lett.*, 2025, **25**, 443–452.
133 J. Yu, J. Li, C.-Y. Xu, Q. Li, Q. Liu, J. Liu, R. Chen, J. Zhu and J. Wang, *Nano Energy*, 2022, **98**, 107266.
134 S. Nagappan, H. Minhas, R. R. Urkude, B. Pathak and S. Kundu, *Small*, 2025, **21**, 2500081.
135 B. Song, H. Zhao, G. Zhao, H. Li, C. Ge, G. Yan and J. Fang, *Chem. Eng. J.*, 2023, **460**, 141907.
136 J. Jin, Z. Sun, T. Yan, Z. Shi, M. Wang, T. Huang, Y. Ding, J. Cai, P. Wang, L. Zhang and J. Sun, *Small Sci.*, 2022, **2**, 2200059.
137 G. Zhao, Q. Chen, L. Wang, T. Yan, H. Li, C. Yuan, J. Mao, X. Feng, D. Sun and L. Zhang, *J. Mater. Chem. A*, 2022, **10**, 19893–19902.
138 H. Liu, Q. Xu, Y. Zhang, G. Luo, N. Han, H. Liu and X. Zhang, *Chem. Eng. J.*, 2025, **513**, 163084.
139 Y. Zheng, M. Khan, S. Yan, D. Yang, Y. Chen, L. Zhang, X. Song, G. Li, J. Liu and Y. Wang, *Front. Chem.*, 2024, **12**, 1–10.